




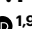


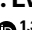

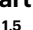

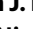
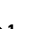

Acoustically activatable liposomes as a translational nanotechnology for site-targeted drug delivery and noninvasive neuromodulation

Received: 23 October 2024

Accepted: 24 June 2025

Published online: 18 August 2025

 Check for updates

Mahaveer P. Purohit ^{1,9}, Brenda J. Yu ^{1,2,9}, Kanchan Sinha Roy ^{1,9}, Yun Xiang ^{1,9}, Sedona N. Ewbank ^{1,3}, Matine M. Azadian^{1,3}, Alex R. Hart ^{1,4}, Gabriella P. B. Muwanga ^{1,3}, Payton J. Martinez ¹, Jeffrey B. Wang ^{1,5}, Ali K. Taoube ¹, Eric Markarian ¹, Nicholas Macedo¹, Audrey K. Kwan ¹, Diego Gomez Lopez^{1,6} & Raag D. Airan ^{1,7,8} ✉

Stimulus-responsive drug delivery nanotechnologies promise noninvasive activation of the right drug at the right place at the right time. However, these systems often incorporate non-validated pharmaceutical excipients and other features that limit their clinical translation. Here we engineer the responsiveness of liposomes to a pulsed, low-intensity ultrasound activating stimulus by incorporating a generally regarded as safe excipient that alters the acoustic properties of the liposome core medium. We show that this approach permits loading and ultrasound-induced release of four drugs *in vitro*. We then leverage this performance to enable drug-mediated noninvasive neuromodulation of each of the central and the peripheral nervous system *in vivo*. These acoustically activatable liposomes formulated with common and validated pharmaceutical excipients and production processes provide a versatile system for stimulus-responsive site-targeted drug delivery and noninvasive neuromodulation, with high clinical translation potential.

Ultrasound-gated drug delivery leverages clinical therapeutic ultrasound systems in clinical use for myriad applications¹ to provide on-demand pharmacology targeting millimetre-sized brain and bodily regions of interest. For ultrasonic drug uncaging, following intravenous infusion of ultrasound-sensitive drug-loaded nanocarriers, focused ultrasound (FUS) applied to a region of interest is sufficient to induce drug uncaging from the nanocarriers while they circulate in the blood or are resident in the parenchyma² (Fig. 1a). The freed drug then enters the otherwise unperturbed parenchyma.

Several ultrasonic drug uncaging nanocarriers have been described, including perfluorocarbon-based systems in which the perfluorocarbon material may inertially cavitate under ultrasound, risking sonoporation or other forms of tissue injury^{3,4}. In addition, since perfluorocarbons are poor solvents generally, the drug is loaded in the particle shell limiting drug loading and risking nonspecific release in the body. While perfluorocarbon double emulsions and gas-containing liposomes load the drug in an aqueous or solvent core, perfluorocarbon double emulsions usually have large (>10 µm) particle sizes preventing

¹Department of Radiology, Stanford University, Stanford, CA, USA. ²Biophysics Program, Stanford University, Stanford, CA, USA. ³Neurosciences Program, Stanford University, Stanford, CA, USA. ⁴Department of Chemistry, Stanford University, Stanford, CA, USA. ⁵Department of Anesthesiology and Critical Care Medicine, John Hopkins Hospital, Baltimore, MD, USA. ⁶Department of Medicine, Health, and Society, Vanderbilt University, Nashville, TN, USA. ⁷Department of Psychiatry and Behavioral Sciences, Stanford University, Stanford, CA, USA. ⁸Department of Materials Science and Engineering, Stanford University, Stanford, CA, USA. ⁹These authors contributed equally: Mahaveer P. Purohit, Brenda J. Yu, Kanchan Sinha Roy, Yun Xiang. ✉ e-mail: rairan@stanford.edu

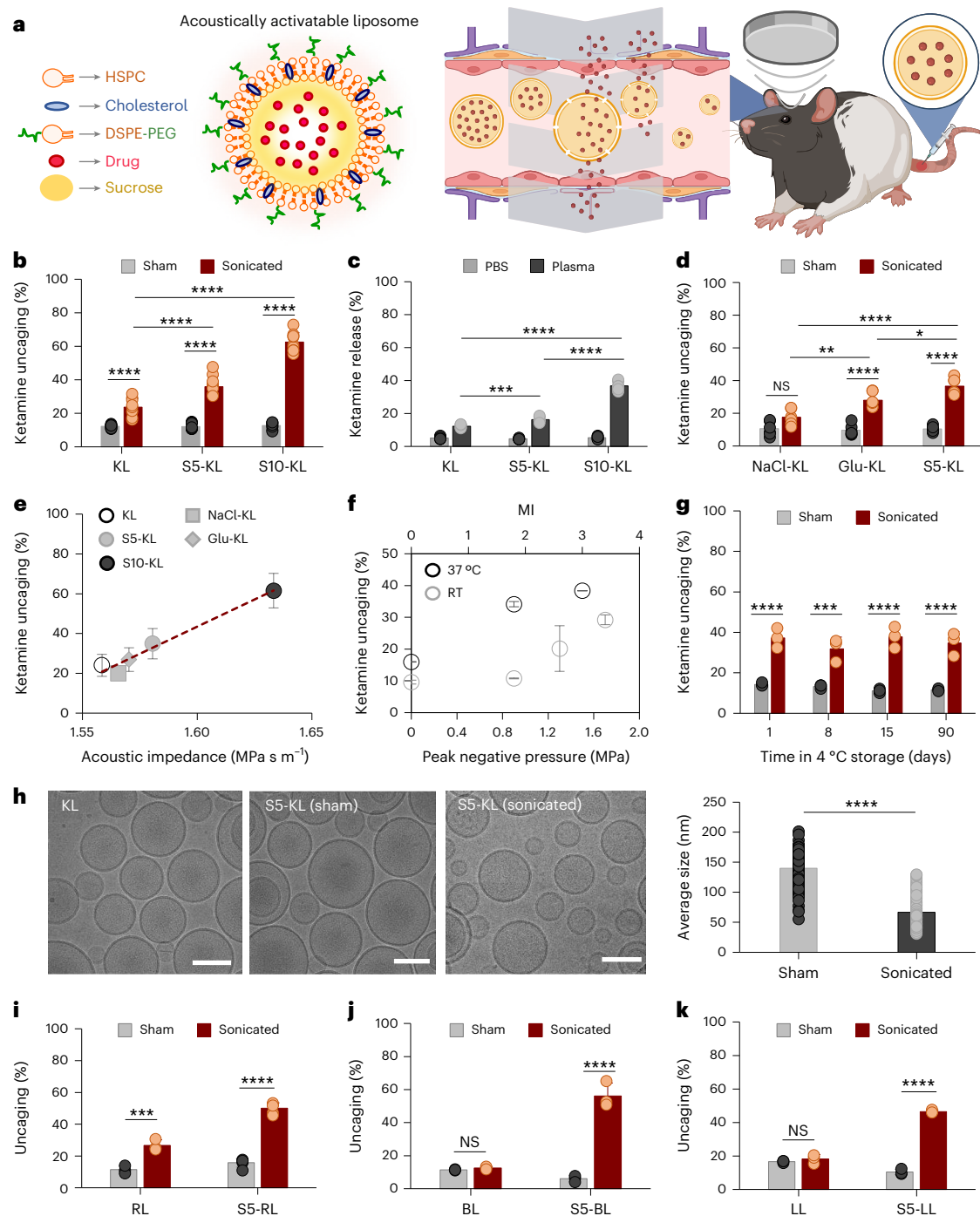


Fig. 1 | AALs for on-demand drug uncaging. **a**, Ultrasound-sensitive drug nanocarriers release their cargo upon ultrasound activation while they are circulating in the blood pool because sucrose alters the liposome internal buffer acoustic characteristics and osmolality, increasing interaction with ultrasound, which increases lipid membrane drug permeability, allowing drug release that is accelerated by the osmotic gradient (<https://biorender.com/bfnjkwv>). **b**, In vitro ketamine uncaging from ketamine-loaded (KL) liposomes with 0% (KL), 5% (S5-KL) or 10% (S10-KL) added sucrose. Sonication (250 kHz centre frequency, 1.7 MPa estimated in situ peak negative pressure at RT, 25% duty cycle, PRF 5 Hz, 60 s) with more sucrose internally uncaged more drug ($n = 9$ per group). **c**, Spontaneous ketamine release from KL, S5-KL and S10-KL with 1 h of 37 °C incubation in plasma or buffer shows 10% additional sucrose yields reduced 37 °C plasma stability ($n = 6$ per group). **d, e**, Bar (**d**) and scatter plots (**e**) of drug uncaging from liposomes with equiosmolar additional sodium chloride (NaCl-KL), glucose (Glu-KL) or sucrose (S5-KL) shows that uncaging performance correlates with internal acoustic impedances differences; $r^2 = 0.97$, $P = 0.002$

($n = 3$ per group) (* $P = 0.0129$, ** $P = 0.0017$). **f**, Ultrasonic ketamine uncaging from S5-KL with varying peak negative pressure/MI (250 kHz, 25% duty cycle, PRF 5 Hz, 60 s) at RT or 37 °C ($n = 3$ per group). **g**, Stability of S5-KL for drug retention and uncaging across 90 days in 4 °C storage. No observed change in size/PDI by DLS; representative batch size/PDI of 165.8 nm/0.061 at day 1 and 167.7 nm/0.074 at day 90 post production ($n = 3$ per group). **h**, Electron microscopy shows spherical shape of the liposomes with primarily unilamellar vesicles and <5% multilamellar vesicles, with particle size decreasing with sonication. No gas elements or voids within the AALs with or without sonication. Scale bars, 100 nm. **i–k**, Ropivacaine (RL; **i**), bupivacaine (BL; **j**) and lidocaine loaded (LL; **k**) liposomes with or without 5% additional sucrose internally show higher in vitro ultrasonic drug uncaging with sucrose incorporation ($n = 3$ per group). Data presented as mean \pm s.d. of three or more independent experiments. Comparisons between two groups were performed by two-tailed, two-sample Student's *t*-test, and that among multiple groups by one-way ANOVA; NS, not significant, * $P < 0.05$, ** $P < 0.01$, *** $P < 0.001$ and **** $P < 0.0001$.

safe intravenous administration⁵ and echogenic liposomes entrap gas yielding instability and risking damaging inertial cavitation under sonication⁶. Alternatively, heat-sensitive liposomes release drug with medium heating⁷. While effective, this heating may induce tissue heat shock and presents technical challenges in highly vascularized tissue, in organs that move with cardiorespiratory motion, and near bony interfaces, with corresponding high actuating device performance requirements⁷. Other liposomes incorporate a porphyrin or related molecule, producing reactive oxygen species under sonodynamic ultrasound inducing therapeutic release⁸. This requires continuous ultrasound for minutes necessitating similar technical constraints as heat-activated liposomes, and was validated using direct intraparenchymal injection. Another ultrasound-responsive liposome uses supercritical carbon dioxide incorporation⁹ with bubble generation under ultrasound, also risking inertial cavitation and instability, as with microbubbles.

We aimed for an ultrasonic drug uncaging vehicle that (1) enables high drug loading of varied drugs of interest, (2) can be activated following intravenous (not intraparenchymal) administration, (3) is formulated with validated pharmaceutical excipients and (4) can be activated with a lower duty cycle, shorter ultrasound protocol than heat or sonodynamic activation. We met this target by designing ultrasound-responsive drug nanocarriers that incorporate excipients that shift the acoustic characteristics of the nanocarrier liquid core to maximize its ultrasound responsiveness while maintaining stability without ultrasound. We have formulated these acoustically activatable liposomes (AALs) with validated pharmaceutical excipients and production processes and confirmed their ultrasonic drug uncaging performance *in vivo* in both the brain and body, confirming their high clinical translational potential.

Design and development of AALs

Towards a next-generation ultrasonic drug uncaging nanocarrier, since our previous liquid perfluorocarbon-based formulation demonstrated no vaporization during effective uncaging^{10,11}, we hypothesized that we could maintain ultrasound sensitivity with improved stability and drug loading by replacing the core perfluorocarbon with an aqueous droplet that has sufficiently different acoustic characteristics versus its surroundings to enable an ultrasound interaction. In addition, if the internal buffer has a sufficiently different osmolarity versus its surroundings, then following the membrane permeability induced by the ultrasound interaction, this osmotic gradient would induce a fluid shift that accelerates drug release (Fig. 1a). Finally, by replacing perfluorocarbons with validated pharmaceutical excipients, we would increase clinical translatability.

To implement this design, we started with liposomes as they are common drug delivery vehicles formulated with validated pharmaceutical excipients¹². We incorporated sugars into the liposome internal core since they are GRAS (generally recognized as safe) excipients¹³ that may shift acoustic properties such as the speed of sound (c) and medium density (ρ), which determine the acoustic impedance ($Z = \rho c$) and bulk modulus ($K = \rho c^2$)^{14,15}. Indeed, with moderate added sugar, the acoustic impedances of standard liposomal internal media shifted between 1.55 MPa s m⁻¹ and 1.65 MPa s m⁻¹ (Extended Data Table 2) compared with 0.0004 MPa s m⁻¹ for perfluorocarbon gas and 0.7–0.9 MPa s m⁻¹ for perfluorocarbon liquids¹⁶.

Loading the anesthetic and antidepressant ketamine (Extended Data Table 1), compared with no added excipient, liposomes incorporating varied percentages of sucrose showed increased ultrasonic drug uncaging, with 5% added sucrose yielding ~40% uncaging and 10% added sucrose yielding ~60% uncaging, compared with a non-significant trend towards ~20% drug uncaging with no added sucrose (Fig. 1b). The lack of 100% drug release likely reflects our limiting of ultrasound parameters to those most relevant for *in vivo* application, floor and saturation effects of this assay, inhomogeneity of the applied ultrasound field, reloading of the freed drug before separation for quantification and

heterogeneity of the liposomal particles' response to ultrasound. Sucrose incorporation yielded no differences in physicochemical properties such as size, polydispersity, zeta potential, drug loading or unencapsulated drug (Extended Data Table 1). However, while 10% additional sucrose increased uncaging efficacy relative to 5% additional sucrose, it also increased drug release without ultrasound during 37 °C plasma incubation, indicating a trade-off of ultrasound responsiveness and stability with this scheme (Fig. 1c).

As sucrose incorporation shifts both acoustic parameters and osmolarity, to discern which contributed more to uncaging, we prepared liposomes with equiosmolar internal buffers but varying acoustic parameters (Extended Data Table 2). Drug-loaded liposomes with equiosmolar additional sodium chloride, glucose or sucrose had similar physicochemical characteristics with each other (Extended Data Table 1) yet showed differing drug uncaging under the same ultrasound protocol, in correlation to their acoustic impedance (Fig. 1d,e and Extended Data Table 2), indicating that differential acoustic characteristics, rather than another physical parameter, most contribute to ultrasound responsiveness. Hyperosmolarity of the internal medium may contribute to a baseline leak or instability (Fig. 1c) or accelerates drug release by driving water influx following ultrasound-increased membrane permeability. Going forward, 5% added sucrose was chosen for its balance of ultrasound responsiveness and formulation stability.

With 5% added sucrose, *in vitro* dose–response relationships were noted of drug uncaging with ultrasound parameters such as *in situ* peak negative pressure and mechanical index (MI; Fig. 1f). There was increased uncaging at 37 °C versus room temperature (RT) (–22 °C; Fig. 1f), although the response at RT indicates that medium heating is not necessary for uncaging performance. In addition, at these intensities and duty cycles, ultrasound-induced medium heating is at most +0.1–0.2 °C per the bio-heat equation¹⁷, arguing against a thermal mechanism. Indeed, when varying ultrasound frequency, we observed that uncaging scaled with MI more than the pressure (Extended Data Fig. 1a,b), indicating that radiation force and heating do not substantially contribute to the uncaging mechanism, as they require lower or similar intensities at higher frequencies. Instead, a mechanical (oscillatory or cavitation) mechanism appears more likely—albeit with low risk of damaging inertial cavitation as the liposomes do not contain gas. When recording acoustic backscatter and emissions during sonication, we readily observed broadband signal offset, ultraharmonics and band widening with microbubbles and did not see these signals with the liposome internal buffer or liposomes versus saline across MI = 0.6–3.0 (Extended Data Fig. 1c). Instead, with higher sonication pressures, the liposome internal medium and liposomes showed differential scatter compared with saline, consistent with a reflection from the flow tubing containing these media of different acoustic impedances (Extended Data Table 2) and a high concentration of scattering particles for the liposomes. Aside from this nonspecifically increased scatter, we observed no specific signs of inertial cavitation (ultraharmonics, subharmonics, band widening and so on) over saline of these liposomes or the liposome internal buffer for sonication up to 1.5 MPa, well above the pressure needed for effective drug release and what would be used *in vivo*. To investigate potential cavitation-related bioeffects *in vivo*, commercial microbubbles or AALs were infused intravenously in rats with co-administered Evans Blue dye, and sonication was applied transcranially to the rodent brain. For liposomes, sonication that is more than sufficient for drug uncaging was used. For microbubbles, a lower intensity and duty cycle protocol typical for blood–brain barrier disruption experiments was used. While Evans Blue extravasation was readily observed with microbubble sonication, indicating blood–brain barrier disruption, no blood–brain barrier disruption or other cavitation-related tissue change was seen with liposomes (Extended Data Fig. 1d). Regarding heating, simulations indicate that no substantial tissue parenchymal heating would be observed and experimental observations demonstrated at most minimal heating

at the skull bony interface with an ultrasound protocol sufficient for uncaging (Extended Data Fig. 3d), further supporting that a thermal uncaging mechanism is not necessary.

Importantly, this formulation shows stability for both drug loading and ultrasonic uncaging across months of refrigerated storage (Fig. 1g). By electron microscopy, the formulation particles show the expected spherical morphology (Fig. 1h) and decreased in size with sonication, cohering with ultrasound-induced internal content leak (Fig. 1h). Importantly, no gas bubbles or voids were noted within the liposomes with or without sonication. Effective uncaging was seen at body temperature with 250 kHz ultrasound and an in situ peak negative pressure of 0.9 MPa, MI = 1.8, within FDA and iTRUSST guidelines for safe ultrasound application^{18,19}.

To explore this platform's generalizability, we prepared liposomes with or without 5% additional sucrose and loaded with lidocaine, bupivacaine and ropivacaine: local anaesthetics that would enable non-invasive peripheral neuromodulation (complementing the central neuromodulation offered by ketamine uncaging) and provide a range of chemical features (logP and pKa) that may differentially affect loading. The ammonium sulfate-based method that we used allows high drug loading of amphiphilic weak basic drugs, particularly those of appropriate size, polarity and logP of their nonionized species to permit passive transit through a lipid bilayer, and of pKa so that an acidic environment yields protonation of the drug to trap it internally¹². Notably, these features are similar to those that permit passive transport across the blood–brain/nerve barrier. This ultrasonic uncaging strategy may work for any therapeutic compound that may be stably loaded into liposomes, whether loading is active with this or another chemical battery, or if the loading is passive. These local anaesthetic-loaded liposomes showed similar size, polydispersity and zeta potential as the ketamine-loaded liposomes (Extended Data Table 1). They showed differential drug loading reflecting their chemical characteristics (logP and pKa) as they relate to the ammonium sulfate active loading mechanism (Extended Data Table 1). Increased uncaging was observed with added sucrose internally (Fig. 1i–k), confirming the generalizability of this design for ultrasound-responsive nanocarriers. Each liposome showed the expected spherical morphology, with a liquid core with no observable gas or voids (Extended Data Fig. 1e).

In vivo AAL-mediated ultrasonic drug uncaging performance

For characterizing AAL performance in vivo, we normalized dose by drug mg kg⁻¹ between unencapsulated and liposomal formulations as the safety profile, pharmacokinetics and pharmacodistribution of drugs are usually reported as functions of total dose rather than a target site concentration. Following a dose-matched intravenous bolus, there were differential blood pharmacokinetics between AAL and unencapsulated drug formulations (Extended Data Fig. 4a and Extended Data Table 3) and higher drug metabolite blood levels with the AAL formulation versus unencapsulated drug. At 1 h post administration, solid organs showed increased accumulation of the drug with the unencapsulated formulation compared with the AAL (Extended Data Fig. 4b). The combination of higher blood drug metabolite concentration yet lower solid organ unmetabolized drug accumulation with the AAL formulation suggests that some clearance of the AAL formulation is likely due to sequestration and metabolism of the whole particle by organs such as the liver. Further, this end organ sequestration and metabolism could contribute to nonspecific leak of the unmetabolized drug and may be a less present mechanism in humans versus rodents given the lower human weight-normalized hepatic blood flow and mass.

To assess the pharmacodistribution achieved with AAL ultrasonic drug uncaging, in adult rats, we used solid-phase microextraction (SPME) following unencapsulated drug or liposome infusion, with or without ultrasound application to the brain²⁰. Ultrasound (or sham) was applied to a frontal region unilaterally during intravenous infusion

of either unencapsulated ketamine HCl (KetHCl) or ketamine-loaded liposomes (Fig. 2a). After treatment, we stereotactically sampled both the sonicated brain and a contralateral control region 5 mm apart. Craniectomies were performed to enable brain SPME sampling; for non-SPME experiments (Figs. 4 and 5) sonication was completed fully transcranially. The transducer lateral FWHM (full-width at half-maximum) is 7.4 mm (Extended Data Fig. 2) and the axial focal length (50%, FWHM) is 18.6 mm, which covers the full dorsal–ventral axis of the rat brain allowing control sampling only lateral to the focus and not axially. Varying ultrasound parameters or total AAL dose demonstrated dose–response relationships of the amount of drug delivered (Fig. 2b,c). No similar dose–response relationship was observed for control/sham site drug concentration, reflecting a floor effect of SPME (Supplementary Fig. 1) that likely overestimates the true in vivo nonspecific drug release rate.

Blood samples showed higher blood ketamine levels with each liposomal formulation compared with unencapsulated drug, confirming our bolus pharmacokinetics (Fig. 2d and Extended Data Fig. 4a). Despite this higher blood ketamine concentration with liposomes, the ketamine brain levels with sham or in the control region were less than half that of dose-matched free ketamine (Fig. 2e). While ultrasound did not alter the pharmacodistribution following free ketamine infusion, ultrasound yielded higher brain ketamine levels with the liposomes compared with sham or the contralateral non-sonicated region, confirming the performance of this technique and a <5 mm spatial resolution (Fig. 2a,e), just over half the FWHM of this 250 kHz transducer (Extended Data Fig. 2), confirming that AAL-mediated drug delivery is limited spatially by the applied ultrasound field. Furthermore, higher brain ketamine levels were seen with sonication with liposomes with additional sucrose compared with liposomes without added sucrose, confirming that this simple manipulation increases the ultrasound sensitivity both in vitro and in vivo. Despite higher uncaging in vitro, no difference was seen in vivo between liposomes made with 10% versus 5% added sucrose, likely reflecting the instability of the 10% added sucrose formulation (Fig. 1b,c). Histology showed no brain parenchymal injury with AAL-mediated ultrasonic drug uncaging (Fig. 2f–j), arguing against an unsafe degree of inertial cavitation (Extended Data Fig. 1) or tissue heating (Extended Data Fig. 3c,d) with these AAL and ultrasound doses that are effective for spatially localized ultrasound targeted drug delivery in vivo.

Selecting the activity of ketamine with regional uncaging

We next enabled site-specific pharmacologic noninvasive neuromodulation with ketamine uncaging²¹. We selected the 5% sucrose AAL (S5-KL) as an optimum for uncaging performance in vitro and in vivo (Figs. 1 and 2) and denoted it SonoKet. We targeted ketamine delivery to brain regions important for mediating its affective (medial prefrontal cortex (mPFC))²² and dissociative (retrosplenial cortex (RsC))²³ actions (Fig. 3a and Extended Data Fig. 3a,b). During 1.5 mg kg⁻¹ SonoKet or free KetHCl infusion for 5 min, ultrasound or sham was applied to either the mPFC or RsC during the last 2.5 min of infusion.

While ultrasound did not affect the pharmacodistribution of unencapsulated KetHCl (Fig. 3b,c), with SonoKet there was selectively increased delivery in the sonicated brain regions (mPFC, 2.1×; RsC, 2.0×) with no difference in the non-sonicated brain region versus sham, and no difference of delivery or clearance between mPFC and RsC (Fig. 3b,d). With SonoKet uncaging, there was higher ketamine delivery versus dose-matched free KetHCl (mPFC, 1.2×; RsC, 1.5×; Fig. 3b). Sonicated regions consistently had twofold or higher delivery than non-sonicated regions, providing a suitable therapeutic window, noting that this delivery rate without ultrasound is likely an overestimate given an SPME floor effect (Supplementary Fig. 1). Importantly, each experiment showed a similar clearance profile, with ketamine and its metabolites clearing by 15–20 min post-treatment (Fig. 3c–e,

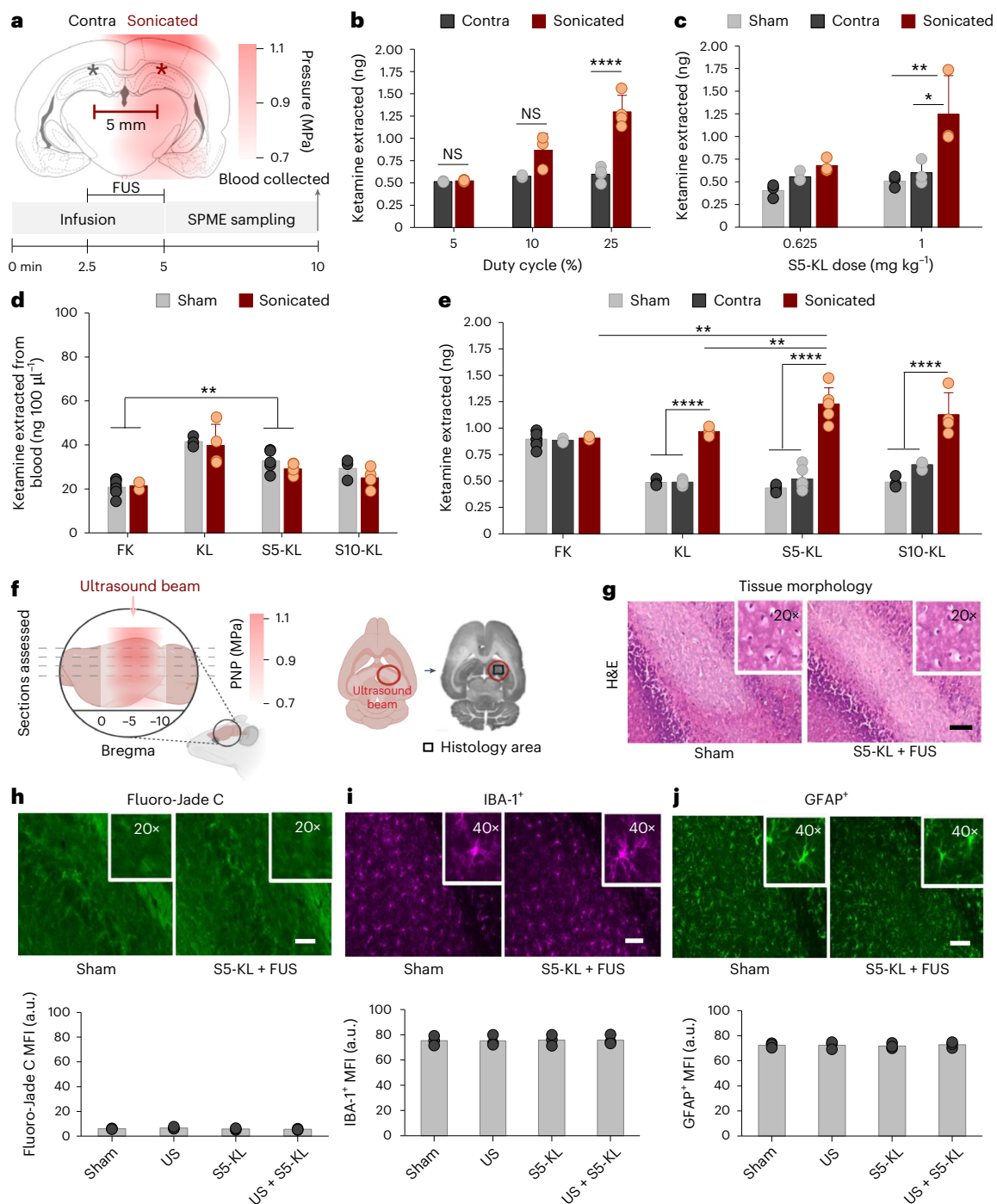


Fig. 2 | In vivo AAL uncaging performance and spatial resolution. **a**, Ultrasound (250 kHz, 0.9 MPa estimated peak in situ negative pressure (PNP) at sampling target, 5–25% duty cycle, 5 Hz PRF) or sham was applied unilaterally following intravenous infusion of 0.625–1.5 mg kg⁻¹ body weight of free KetHCl (FK) or ketamine liposomes with 0% (KL), 5% (S5-KL) or 10% (S10-KL) added sucrose. Hydrophone beam map informed simulations of the transducer sonicating across rat skull with intensity derated for rat skull insertion loss overlaid on rat brain atlas targets⁴². After sonication, SPME sampled both sonicated brain (red asterisk) and a contralateral control (Contra; black asterisk) separated 5 mm. A venous blood sample was then taken. **b**, Increasing ketamine from the sonicated (red) target with increasing ultrasound parameters; with no change in contralateral control (Contra; grey) levels. **c**, Increasing ketamine from the sonicated (red) target with increasing AAL dose; with no change in contralateral control (Contra; grey) or sham (light grey) levels (* $P = 0.0125$, ** $P = 0.0047$). **d**, Ketamine blood levels were higher with the liposomes (KL, S5-KL and S10-KL) compared with dose-matched free drug (FK). **e**, With free ketamine (FK) no change in pharmacodistribution with

ultrasound. With liposomes, ultrasound increased the brain drug concentration at the sonicated target versus contralateral or sham controls, with increased uncaging with sucrose incorporation (FK sonicated versus S5-KL sonicated $P = 0.0084$, KL sonicated versus S5-KL sonicated $P = 0.0055$). **f**, Histologic safety analysis schematic of the rat brain 72 h after sonication with AALs ($n = 3$ per group) shows no indication of parenchymal damage compared with healthy controls (<https://BioRender.com/dul0r3t>). **g**, Representative images of H&E (4x large, 20x inset) staining from the topmost schematic section show no tissue and cellular morphology change. **h–j**, Representative images (top row; 10x, large, 20x for **h**, 40x for **i**, **j**, inset) from the topmost schematic section of Fluoro-Jade C staining for neurodegeneration (**h**), IBA-1 immunostaining for microglial activation (**i**) and GFAP immunostaining for gliosis (**j**) show no change; quantification in bottom row. MFI, mean fluorescence intensity. Scale bars, 100 µm. Data presented as mean \pm s.d. Comparisons between two groups were performed by two-tailed Student's *t*-test, and that among multiple groups by one-way ANOVA; group n , 3–8. * $P < 0.05$, ** $P < 0.01$, *** $P < 0.001$ and **** $P < 0.0001$.

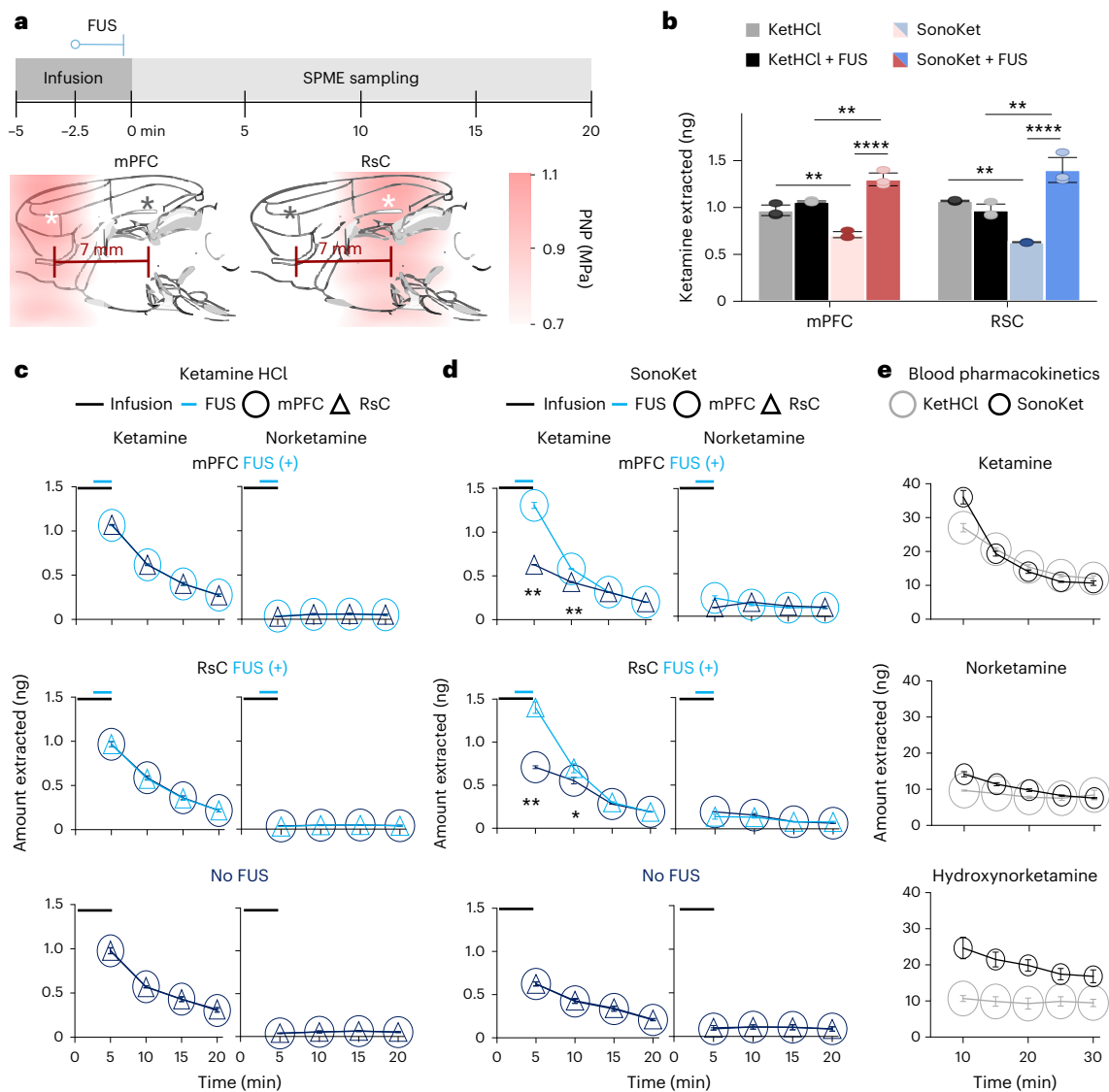


Fig. 3 | In vivo ketamine AAL uncaging at functionally relevant regions. **a**, Top: rats received 1.5 mg kg⁻¹ intravenous of ketamine-loaded AALs (SS-KL from prior, now SonoKet; *n* = 3) or dose-matched KetHCl (*n* = 3) for 5 min, with sonication (FUS) at *t* = 2.5–5.0 min or no sonication (*n* = 5). Bottom: simulated (Extended Data Fig. 3) ultrasound beamplots overlaid onto mPFC (mediates affective ketamine responses) or RsC (mediates dissociative ketamine responses) targets (sagittal brain drawings made new for this figure with cross-reference to the Paxinos atlas⁴³ to ensure accuracy). SPME sampling targets indicated as white asterisk = sonication on, black asterisk = no sonication with sampling every 5 min for 25 min post-infusion start. **b**, Initial ketamine levels show higher ketamine from both mPFC and RsC with SonoKet sonication versus KetHCl or SonoKet without sonication. mPFC: KetHCl versus SonoKet (*P* = 0.0028, Hedges *g* = 3.66); KetHCl + FUS versus SonoKet + FUS (*P* = 0.0041, Hedges *g* = 3.24); SonoKet versus SonoKet + FUS (*P* = 7 × 10⁻⁶, Hedges *g* = 7.31). RsC: KetHCl versus SonoKet

(*P* = 0.0016, Hedges *g* = 45.46); KetHCl + FUS versus SonoKet + FUS (*P* = 0.0018, Hedges *g* = 2.69); SonoKet versus SonoKet + FUS (*P* = 2.99 × 10⁻⁵, Hedges *g* = 5.37). One-way, two-sided, ANOVA and Tukey's post hoc HSD, **P* < 0.05, ***P* < 0.01, ****P* < 0.001 and *****P* < 0.0001. **c**, No difference in pharmacodistribution or pharmacokinetics of ketamine or norketamine with free ketamine and sonication at either target. Hydroxynorketamine levels below limit of detection. Paired *t*-tests, two-sided. **d**, Ketamine and norketamine brain levels and clearance with SonoKet show higher brain ketamine with sonication applied to mPFC (top left; 5 min, *P* = 0.0043, 10 min, *P* = 0.0057) or RsC (middle left; 5 min, *P* = 0.010, 10 min, *P* = 0.022) versus non-sonicated regions. Similar clearance rate in both regions. Hydroxynorketamine levels below limit of detection. Paired *t*-tests, two-sided, **P* < 0.05 and ***P* < 0.01. **e**, Blood pharmacokinetics of ketamine, norketamine and hydroxynorketamine; modelling results in Extended Data Table 3. Paired *t*-tests, two-sided. Data presented as mean ± s.d.

Extended Data Fig. 4 and Extended Data Tables 3 and 4). While ketamine's metabolites have been proposed as pivotal to its actions, their brain levels were negligible compared with unmetabolized ketamine, with no differences of metabolite distribution or clearance with free or SonoKet-encapsulated ketamine (Fig. 3c–e, Extended Data Fig. 4 and Extended Data Tables 3 and 4). Importantly, the biodistribution analyses demonstrate lower solid organ ketamine uptake with SonoKet administration versus dose-matched unencapsulated ketamine (Extended Data Fig. 4b), confirming that ultrasonic ketamine uncaging should lower systemic side effects while selectively delivering

ketamine to these functionally significant brain targets, with otherwise similar pharmacokinetics compared with unencapsulated ketamine.

To evaluate the functional efficacy of localized ketamine delivery in the context of acute stress, we measured electrocorticography (ECoG) over the mPFC and RsC while awake subjects were in a restraint that induces acute stress in rodents²⁴ (Fig. 6a). Different ECoG oscillation patterns have been associated with different ketamine actions, with frontal gamma band activity being a biomarker of affective action²⁵ and retrosplenial slower band activity correlated to dissociation^{23,26}. ECoG potentials were processed to determine

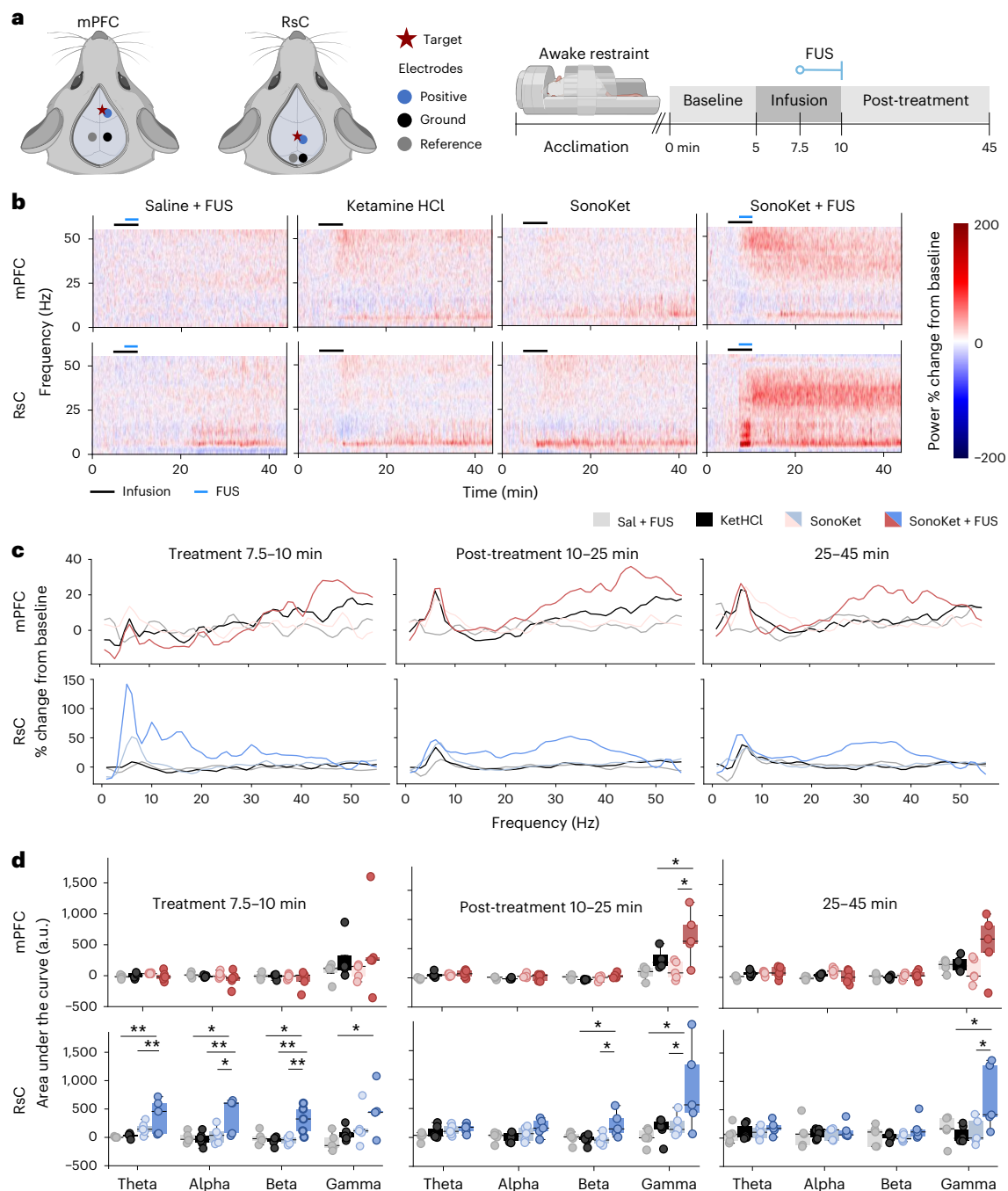


Fig. 4 | Unique electrophysiologic signatures of AAL-mediated regional ketamine uncaging. **a**, Schematic (left) and timeline (right) of 45 min recording from fully awake rats undergoing acute restraint stress. Following 5 min baseline, intravenous infusion administered $t = 5-10$ min and FUS (250 kHz; 1.1 MPa estimated in situ peak negative pressure; 50 ms/5 Hz PRF/2.5 min) applied $t = 7.5-10$ min (<https://BioRender.com/u2nnlio> and <https://BioRender.com/byb05hr>). **b**, Spectrograms depicting electrophysiological response to saline with ultrasound and free KetHCl (0.75 mg kg⁻¹; repeated from dose-response evaluation; Extended Data Fig. 5), SonoKet (0.75 mg kg⁻¹) without ultrasound, and SonoKet with ultrasound applied to and recording from mPFC (top row; $n = 4-5$) or RsC (bottom row; $n = 5-6$). Power spectral density percent changes from the baseline (0-5 min) were calculated. **c**, Power spectral density percent change from baseline versus frequency for time of sonication (7.5-10 min), immediately after treatment (10-25 min) and in a delayed period (25-45 min). **d**, Power spectral density percent change from baseline area under the curve for each time period and spectral band: theta (4-8 Hz), alpha (8-15 Hz), beta

(15-25 Hz) and gamma (25-55 Hz). mPFC post-treatment, gamma: Sal + FUS versus SonoKet + FUS ($P = 0.0156$); SonoKet versus SonoKet + FUS ($P = 0.0179$). RsC treatment, theta: Sal + FUS versus SonoKet + FUS ($P = 0.0081$); KetHCl versus SonoKet + FUS ($P = 0.0085$). Alpha: Sal + FUS versus SonoKet + FUS ($P = 0.0183$); KetHCl versus SonoKet + FUS ($P = 0.0076$); SonoKet versus SonoKet + FUS ($P = 0.0376$). Beta: Sal + FUS versus SonoKet + FUS ($P = 0.0136$); KetHCl versus SonoKet + FUS ($P = 0.0028$); SonoKet versus SonoKet + FUS ($P = 0.0047$). Gamma: Sal + FUS versus SonoKet + FUS ($P = 0.0231$). RsC post-treatment, beta: KetHCl versus SonoKet + FUS ($P = 0.0271$); SonoKet versus SonoKet + FUS ($P = 0.0365$). Gamma: KetHCl versus SonoKet + FUS ($P = 0.0431$); SonoKet versus SonoKet + FUS ($P = 0.0177$). RsC 25-45 min, gamma: KetHCl versus SonoKet + FUS ($P = 0.0487$). Data presented as box plots show minima, maxima, interquartile range (box bounds) and median (black line). One-way, two-sided, ANOVA followed by Tukey's post hoc HSD for multiple comparisons, * $P < 0.05$ and ** $P < 0.01$.

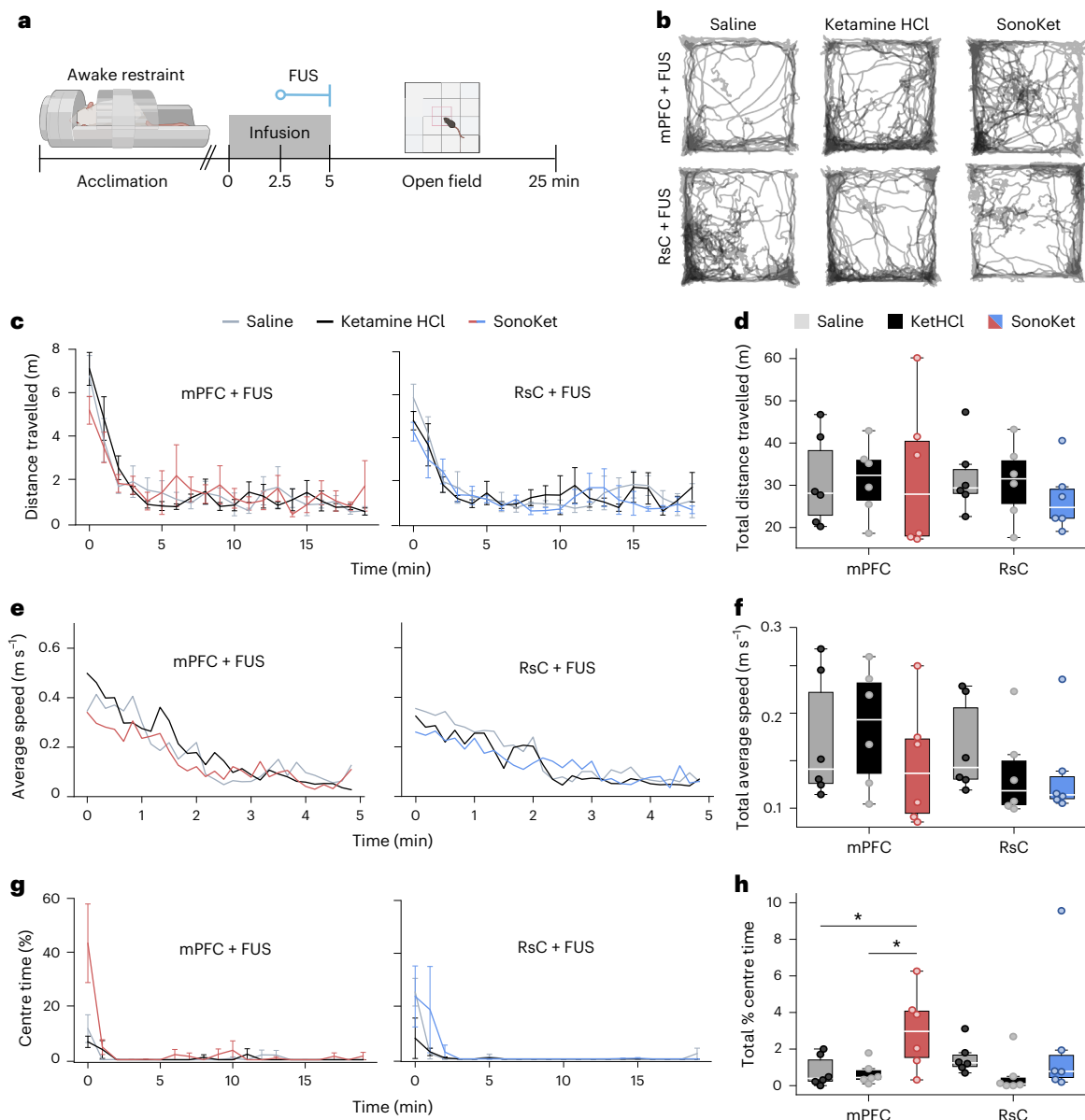


Fig. 5 | Regional AAL-mediated ketamine uncaging selectively activates site-differential behavioural efficacy. **a**, Rats undergoing awake restraint-induced acute stress were administered intravenously either SonoKet (0.75 mg kg^{-1}), dose-matched KetHCl or saline for 5 min, with fully transcranial sonication applied to either the mPFC or RsC at $t = 2.5\text{--}5 \text{ min}$. Rats were then released and placed in an open-field test box and filmed from above in a well-lit room (<https://BioRender.com/59296sm>). **b**, Tracks for all rats overlaid for each group, by treatment and sonicated region. All treatment groups received ultrasound at either the mPFC (top) or RsC (bottom). **c,d**, Total distance travelled within each treatment group averaged across subjects (one recording per animal) in 1 min time bins plotted across time (**c**) and averaged across the entire recording (**d**). Data presented as box plots. One-way, two-sided, ANOVA followed by Tukey's post hoc HSD for multiple comparisons showed no significant differences; $n = 6$ rats per group. **e,f**, Average speed over the first 5 min of recording for each

treatment group averaged across subjects plotted across time (**e**) and averaged across the first 5 min of recording (**f**). Data presented as box plots. One-way, two-sided, ANOVA followed by Tukey's post hoc HSD for multiple comparisons showed no significant differences; $n = 6$ rats per group. **g,h**, Percentage of time spent in the centre versus edge of the field for each treatment group averaged across subjects (one recording per animal) in 1 min time bins plotted across time (**g**) and averaged across the entire recording (**h**). mPFC: saline versus SonoKet ($P = 0.037$, Hedges $g = 1.24$); KetHCl versus SonoKet ($P = 0.028$, Hedges $g = 1.35$). RsC: no significant differences. Data presented as line plots are presented as mean \pm s.e. Data presented as box plots show minima, maxima, interquartile range (box bounds) and median (white line). One-way, two-sided, ANOVA followed by Tukey's post hoc HSD for multiple comparisons; $*P < 0.05$; $n = 6$ rats per group.

the power spectral density across 1–55 Hz before, during and after treatment following similar analyses of intracranial recordings from humans receiving ketamine²⁷.

We first characterized the dose–response relationship for unencapsulated KetHCl and found that there was dose-dependent increased gamma (25–55 Hz) power for both the mPFC and RsC (Extended Data Fig. 5 and Supplementary Fig. 1) and decreased slower band power

for the RsC (Supplementary Fig. 1). The sustained gamma response for the 45 min recordings despite the relatively rapid ketamine clearance (Fig. 3c,e and Extended Data Fig. 4) was expected given previous characterizations²⁸.

During antidepressant ketamine treatment, 0.5 mg kg^{-1} of ketamine infused over 40 min results in plasma ketamine levels of $\sim 200 \text{ ng ml}^{-1}$ in adult humans²⁹, similar to rat plasma ketamine levels

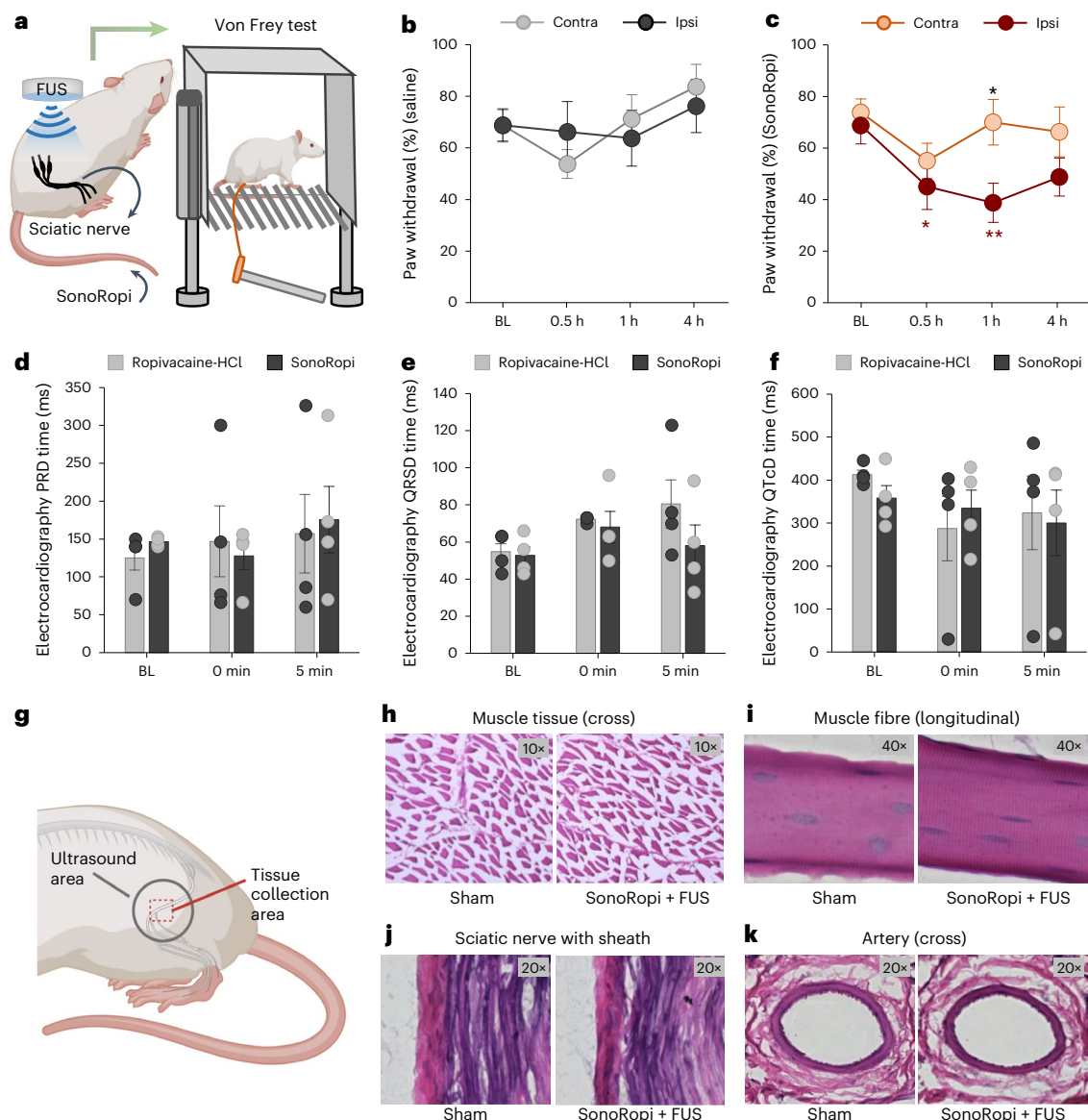


Fig. 6 | Noninvasive nerve block with in vivo AAL-mediated ultrasonic ropivacaine uncaging. **a**, Adult rats ($n = 8$ per group) received a 5 min intravenous infusion of saline or a ropivacaine-loaded AAL (SS-RL from prior, now SonoRopi; 5 mg kg^{-1}), with FUS (250 kHz, 25% duty cycle, 5 Hz PRF, 0.9 MPa estimated in situ peak negative pressure) applied externally transcutaneously to target the sciatic nerve of the left limb for 2.5 min during the latter half of a 5 min infusion. Frequency of paw withdrawal to a mechanical stimulus (von Frey test) was assayed before and after infusion and sonication (<https://BioRender.com/dixj6am>). **b**, In saline- and FUS-treated animals, no significant difference in mechanical sensitivity was seen across time or between the limb ipsilateral (ipsi) to sonication versus the limb contralateral (contra) to sonication. **c**, In SonoRopi- and FUS-treated animals, significant differences in mechanical sensitivity were seen in the limb ipsilateral to sonication at certain time points after sonication and infusion versus the baseline (red asterisks; BL versus

0.5 h $P = 0.0175$, BL versus 1 h $P = 0.0018$), and between the limb ipsilateral to sonication versus contralateral to sonication (black asterisks; $P = 0.0105$). **d–f**, Electrocardiographic parameters recorded at baseline (BL), at the start of infusion (0 min) and the end of infusion (5 min) of 5 mg kg^{-1} ropivacaine-HCl or SonoRopi ($n = 3$ per group) show no significant differences of PR interval duration (PRD; **d**), QRS interval duration (QRS; **e**), and corrected QT interval duration (QTcD; **f**). **g–k**, Schematic (**g**) and representative images (**h–k**) for histological safety analysis with H&E staining of rats receiving the indicated treatment to the sciatic nerve of rats ($n = 3$ rats per group) showed no concerning parenchymal damage when analyzing muscle tissue in the region of interest in cross section (**h**) and longitudinally (**i**), or analyzing the treated sciatic nerve (**j**) and the nearby femoral artery (**k**). (<https://biorender.com/b3028oe>). Data presented as mean \pm s.e. (**b,c**) or s.d. (**d–f**). Comparisons between multiple groups performed by two-way ANOVA; * $P < 0.05$, ** $P < 0.01$ and *** $P < 0.001$.

seen with 0.75 mg kg^{-1} of SonoKet infused over 5 min (Figs. 2 and 3, Extended Data Fig. 4 and Extended Data Tables 3 and 4). We therefore selected 0.75 mg kg^{-1} as the dose going forward. In the awake restraint that can act as an acute stressor²⁴ (Fig. 4a, Extended Data Fig. 5 and Supplementary Fig. 1), rats were administered SonoKet with and without sonication, dose-matched KetHCl or saline with sonication in a random ordering with at least 1 week for washout between experiments. No significant ECoG change was seen with SonoKet

infusion without ultrasound application versus saline. However, with mPFC ketamine uncaging, gamma power increases were observed to a trend-wise greater degree and similar spectral pattern compared with dose-matched free ketamine (Fig. 4b–d and Extended Data Fig. 5). By contrast, with RsC ketamine uncaging, acute increases in principally slower theta (4–8 Hz), alpha (8–15 Hz) and beta (15–25 Hz) bands were observed with then sustained activities in beta and low gamma bands, in a distinct spectral pattern to both dose-matched unencapsulated

ketamine and mPFC uncaging (Fig. 4b–d, Extended Data Fig. 5 and Supplementary Figs. 3 and 4). While RsC SonoKet uncaging showed apparent delta power increases (Fig. 4b,c and Supplementary Fig. 3), cohering with previous characterizations^{23,27}, this may have been driven by changes in the saline condition, suggesting a nonspecific effect of this experimental paradigm. Site specificity was supported by sonication directed to the mPFC while recording from the RsC and vice versa sonication directed to the RsC while recording from the mPFC (Extended Data Fig. 6), as each yielded a different band pattern compared with recording and sonicating both at mPFC or recording and sonicating both at RsC. Sonication at mPFC while recording from RsC showed less gamma activity that was less sustained than recording and sonicating both at mPFC, and no appreciable low-frequency induction and less prominent beta induction compared with recording and sonicating both at RsC. Meanwhile, sonicating at RsC and recording from mPFC showed less high-frequency beta/gamma induction compared with sonicating and recording both from mPFC, and showed less prominent low-frequency induction, with a longer-term decrease in lower band power compared with sonicating and recording both from RsC. Similarity of these patterns may reflect volume transmission of EEG/ECOG signals³⁰ or the known functional connectivity between these regions³¹. These data confirm the functional site specificity of AAL uncaging, in correlation to its site-specific pharmacodistribution (Figs. 2 and 3). Overall, this differential functional electrophysiologic response to ketamine uncaging in the mPFC versus RsC, despite similar levels of ketamine delivery to each brain region, and to greater effect at either site compared with dose-matched unencapsulated ketamine (Fig. 3), confirms the site-specific physiologic action underlying ketamine's multiple functional effects.

For evaluating the behavioural effects of site-targeted ketamine uncaging, despite variability of rodent behavioural responses to subanaesthetic ketamine that may not have human parallels^{32,33}, certain rodent behaviours are indicative of relevant circuit activities. In rodents, ketamine induces locomotion correlated to mesolimbic dopaminergic circuit modulation³³ and stress and affect-related effects correlated to limbic circuit activity²². To evaluate both functional domains, we used the open-field test and quantified parameters related to locomotion and stress/affective processing. Rats were placed in a restraint while awake to induce a brief, acute stress (Fig. 5a), received either saline, unencapsulated KetHCl or SonoKet with sonication directed to either the mPFC or RsC, and then placed in an open field for 20 min. There were no effects on locomotion (Fig. 5b–f and Supplementary Figs. 5 and 6), cohering with previous results demonstrating limited contribution of frontal circuits to ketamine's locomotor effects³⁴. By contrast, mPFC ketamine uncaging yielded more time in the field centre versus dose-matched unencapsulated ketamine or saline (Fig. 5b,g,h; multiple comparison corrected *P* values, saline versus SonoKet *P* = 0.037, Hedges *g* = 1.24; KetHCl versus SonoKet *P* = 0.028, Hedges *g* = 1.35), with no differences seen with RsC uncaging. The lack of locomotion induction coheres with previous similar dose studies and indicates no mesolimbic dopaminergic modulation³⁵. Meanwhile, increased centre time—interpreted as a lower stress, anxiolytic-like phenotype—specifically with mPFC ketamine uncaging coheres with the identification of the mPFC as critical to the affective efficacy of ketamine^{22,36}.

Noninvasive nerve block via ultrasonic ropivacaine uncaging

After confirming that ketamine uncaging yields central neuromodulation (Figs. 3–5), we implemented uncaging-mediated peripheral neuromodulation by targeting local anaesthetics to a peripheral nerve as a noninvasive version of nerve block procedures completed routinely for pain therapy and anaesthesia³⁷ (Fig. 1a). We uncaged an AAL loaded with the local anaesthetic ropivacaine to induce anaesthesia of the rat sciatic nerve. Adult rats were administered a 5 min intravenous infusion

of either saline or a ropivacaine-loaded AAL (SonoRopi, previously denoted SS-RL; Fig. 1i). With sonication then applied to the sciatic nerve of one limb, anaesthesia to a mechanical (von Frey fibre) stimulus was observed only in the sonicated limb of the SonoRopi-administered animals, with this anaesthesia lasting >1 h following treatment (Fig. 6a–c). No such change was seen in the saline-treated animals or in the contralateral non-sonicated limb of the SonoRopi-treated animals (Fig. 6b,c). No electrocardiographic abnormalities or visible intolerances were noted with SonoRopi uncaging (Fig. 6d–f). Histology confirmed no parenchymal injury (Fig. 6g–k).

Conclusion

We have validated a vehicle for ultrasonic drug uncaging with high drug loading, minimal drug release without ultrasound and effective drug uncaging with pulsed low-intensity ultrasound both in vitro and in vivo for multiple drugs and bodily regions of interest. We have therefore proved a design scheme for ultrasound-responsive drug delivery nanotechnologies in which the acoustic properties of the drug-loaded nanocarrier core are shifted by adding excipients that increase interactions with applied ultrasound. In this implementation, the acoustic properties of the core most contribute to ultrasound responsiveness, as liposomes made with cores that were equiosmolar but had different acoustic properties showed differential uncaging performance in correlation to their acoustic properties (Fig. 1d,e). While we have used the GRAS excipient sucrose to maximize clinical translatability, an even further ultrasound-responsive vehicle could be achieved with a different excipient that further shifts the core acoustic characteristics. However, care must be taken that this does not destabilize the liposome, as we observed with 10% added sucrose (Fig. 1c). While an ammonium sulfate-based active loading battery was utilized, this strategy should be applicable to any liposome and loading scheme or to polymeric liquid-core nanocarriers.

While there was a nonzero rate of drug leak without ultrasound both in vitro (Fig. 1) and in vivo (Figs. 2 and 3), the observed in vivo ultrasonic uncaging effect sizes (Figs. 2–6) offer a sufficient therapeutic index for each drug tested and are commensurate with or exceed the demonstrated on- versus off-target delivery of benchmark systems. This baseline nonspecific leak potentially reflects the lack of internal precipitation seen with these liposomes (Figs. 1 and 2) or the metabolism of the AAL contributing to drug leak (Extended Data Fig. 4), and may be overestimated owing to a floor effect of the SPME assay that we used (Supplementary Fig. 1). Notably, this potential metabolic effect may be less present in humans given the lower hepatic blood flow and metabolism of humans compared with rodents. Future efforts will reduce this baseline leak while further maximizing ultrasound responsiveness by including materials that increase internal drug binding and further shift the liposome core acoustic parameters.

The pharmacologic central noninvasive neuromodulation demonstrated here underscores the recent interest in repurposing recreational psychotropic drugs such as ketamine for mental health applications³⁸. However, tempering that excitement are concerns regarding the abuse liability, ethics and safety of clinically utilizing potent hallucinogenic recreational drugs^{39,40}. To address these concerns, as an alternative to synthesizing new chemical entities³⁸, this study supports and provides the technological means for an alternative strategy to achieve selective activation of the therapeutic actions of drugs such as ketamine by targeting unmodified drug delivery to the brain regions most critical for the desired action. In principle, a similar approach could be used for myriad neuropsychiatric drugs that have potent therapeutic effects but dose-limiting side effects owing to action at off-target brain or bodily regions. As current approved protocols for drugs such as ketamine in psychiatric care require close clinical monitoring of the patient⁴¹, applying ultrasonic drug uncaging only minimally complicates workflow: adding ultrasound device operation but potentially saving on patient monitoring if dissociative,

sedative and sympathomimetic properties are indeed minimized. In addition, as demonstrated for peripheral neuromodulation via ropivacaine uncaging, this approach more generally maximizes a drug's therapeutic effect over its side effects. These results will be validated in future clinical studies of honing the action of potent neurally active drugs through regionally targeted drug delivery.

Online content

Any methods, additional references, Nature Portfolio reporting summaries, source data, extended data, supplementary information, acknowledgements, peer review information; details of author contributions and competing interests; and statements of data and code availability are available at <https://doi.org/10.1038/s41565-025-01990-5>.

References

- Lipsman, N., Mainprize, T. G., Schwartz, M. L., Hynynen, K. & Lozano, A. M. Intracranial applications of magnetic resonance-guided focused ultrasound. *Neurother. J. Am. Soc. Exp. Neurother.* **11**, 593–605 (2014).
- Wang, J. B. et al. Focused ultrasound for noninvasive, focal pharmacologic neurointervention. *Front. Neurosci.* **14**, 675 (2020).
- Sirsi, S. R. & Borden, M. A. Advances in ultrasound mediated gene therapy using microbubble contrast agents. *Theranostics* **2**, 1208–1222 (2012).
- Pitt, W. G., Hussein, G. A. & Staples, B. J. Ultrasonic drug delivery—a general review. *Expert Opin. Drug Deliv.* **1**, 37–56 (2004).
- Fabiilli, M. L., Lee, J. A., Kripfgans, O. D., Carson, P. L. & Fowlkes, J. B. Delivery of water-soluble drugs using acoustically triggered perfluorocarbon double emulsions. *Pharm. Res.* **27**, 2753–2765 (2010).
- Huang, S.-L. & MacDonald, R. C. Acoustically active liposomes for drug encapsulation and ultrasound-triggered release. *Biochim. Biophys. Acta* **1665**, 134–141 (2004).
- Dou, Y., Hynynen, K. & Allen, C. To heat or not to heat: challenges with clinical translation of thermosensitive liposomes. *J. Control. Release* **249**, 63–73 (2017).
- Rwei, A. Y. et al. Ultrasound-triggered local anaesthesia. *Nat. Biomed. Eng.* **1**, 644–653 (2017).
- Orita, Y. et al. Acoustic-responsive carbon dioxide-loaded liposomes for efficient drug release. *Ultrason. Sonochem.* **94**, 106326 (2023).
- Zhong, Q. et al. Polymeric perfluorocarbon nanoemulsions are ultrasound-activated wireless drug infusion catheters. *Biomaterials* **206**, 73–86 (2019).
- Wang, J. B., Aryal, M., Zhong, Q., Vyas, D. B. & Airan, R. D. Noninvasive ultrasonic drug uncaging maps whole-brain functional networks. *Neuron* **100**, 728–738.e7 (2018).
- Zucker, D., Marcus, D., Barenholz, Y. & Goldblum, A. Liposome drugs' loading efficiency: a working model based on loading conditions and drug's physicochemical properties. *J. Control. Release* **139**, 73–80 (2009).
- Inactive Ingredients in Approved Drug Products Search: Frequently Asked Questions* (FDA, 2025); <https://www.accessdata.fda.gov/scripts/cder/iig/index.cfm>
- Research C. for D. E. and Inactive Ingredients in Approved Drug Products Search: Frequently Asked Questions* (FDA, 2022); <https://www.accessdata.fda.gov/scripts/cder/iig/index.cfm>
- Nithiyantham, S. & Palaniappan, L. Ultrasonic study on some monosaccharides in aqueous media at 298.15K. *Arab. J. Chem.* **5**, 25–30 (2012).
- Strohm, E. M. & Kolios, M. C. Sound velocity and attenuation measurements of perfluorocarbon liquids using photoacoustic methods. In *2011 IEEE International Ultrasonics Symposium* 2368–2371 (IEEE, 2011).
- Nyborg, W. L. Solutions of the bio-heat transfer equation. *Phys. Med. Biol.* **33**, 785–792 (1988).
- Martin, E. et al. ITRUSST consensus on standardised reporting for transcranial ultrasound stimulation. *Brain Stimul.* **17**, 607–615 (2024).
- Marketing Clearance of Diagnostic Ultrasound Systems and Transducers—Guidance for Industry and Food and Drug Administration Staff* (FDA, 2025); <https://www.fda.gov/media/71100/download>
- Lendor, S. et al. Solid phase microextraction-based miniaturized probe and protocol for extraction of neurotransmitters from brains in vivo. *Anal. Chem.* **91**, 4896–4905 (2019).
- Airan, R. Neuromodulation with nanoparticles. *Science* **357**, 465–465 (2017).
- Moda-Sava, R. N. et al. Sustained rescue of prefrontal circuit dysfunction by antidepressant-induced spine formation. *Science* **364**, eaat8078 (2019).
- Vesuna, S. et al. Deep posteromedial cortical rhythm in dissociation. *Nature* **586**, 87–94 (2020).
- Gamaro, G. D. et al. The effects of acute and repeated restraint stress on the nociceptive response in rats. *Physiol. Behav.* **63**, 693–697 (1998).
- Farmer, C. A. et al. Ketamine metabolites, clinical response, and gamma power in a randomized, placebo-controlled, crossover trial for treatment-resistant major depression. *Neuropsychopharmacology* **45**, 1398–1404 (2020).
- Li, D. & Mashour, G. A. Cortical dynamics during psychedelic and anesthetized states induced by ketamine. *NeuroImage* **196**, 32–40 (2019).
- Tian, F. et al. Characterizing brain dynamics during ketamine-induced dissociation and subsequent interactions with propofol using human intracranial neurophysiology. *Nat. Commun.* **14**, 1748 (2023).
- Pinault, D. N-Methyl D-aspartate receptor antagonists ketamine and MK-801 induce wake-related aberrant γ oscillations in the rat neocortex. *Biol. Psychiatry* **63**, 730–735 (2008).
- Shafer, S. StevenLShafer/stanpumpR (2024).
- Van Den Broek, S. P., Reinders, F., Donderwinkel, M. & Peters, M. J. Volume conduction effects in EEG and MEG. *Electroencephalogr. Clin. Neurophysiol.* **106**, 522–534 (1998).
- Barthas, F. & Kwan, A. C. Secondary motor cortex: where 'sensory' meets 'motor' in the rodent frontal cortex. *Trends Neurosci.* **40**, 181–193 (2017).
- Polis, A. J., Fitzgerald, P. J., Hale, P. J. & Watson, B. O. Rodent ketamine depression-related research: finding patterns in a literature of variability. *Behav. Brain Res.* **376**, 112153 (2019).
- Di Ianni, T. et al. Sex dependence of opioid-mediated responses to subanesthetic ketamine in rats. *Nat. Commun.* **15**, 893 (2024).
- Ali, F. et al. Ketamine disinhibits dendrites and enhances calcium signals in prefrontal dendritic spines. *Nat. Commun.* **11**, 72 (2020).
- Hetzler, B. E. & Swain Wautlet, B. Ketamine-induced locomotion in rats in an open-field. *Pharmacol. Biochem. Behav.* **22**, 653–655 (1985).
- Alexander, L., Jelen, L. A., Mehta, M. A. & Young, A. H. The anterior cingulate cortex as a key locus of ketamine's antidepressant action. *Neurosci. Biobehav. Rev.* **127**, 531–554 (2021).
- Cuvillon, P. et al. A comparison of the pharmacodynamics and pharmacokinetics of bupivacaine, ropivacaine (with epinephrine) and their equal volume mixtures with lidocaine used for femoral and sciatic nerve blocks: a double-blind randomized study. *Anesth. Analg.* **108**, 641–649 (2009).
- Cameron, L. P. et al. A non-hallucinogenic psychedelic analogue with therapeutic potential. *Nature* **589**, 474–479 (2021).
- Reardon, S. MDMA therapy for PTSD rejected by FDA panel. *Nature* <https://doi.org/10.1038/d41586-024-01622-3> (2024).

40. Bonaventura, J. et al. Pharmacological and behavioral divergence of ketamine enantiomers: implications for abuse liability. *Mol. Psychiatry* **26**, 6704–6722 (2021).
41. SPRAVATO® (esketamine) | Healthcare Professional Website. *SPRAVATO® (esketamine): A Prescription Nasal Spray* | SPRAVATO® HCP (2025); <https://www.spravatohcp.com/trd-efficacy-safety/>
42. Swanson, L. W. *Brain Maps III: Structure of the Rat Brain* (Gulf Professional Publishing, 2004).
43. Paxinos, G. & Watson, C. *The Rat Brain in Stereotaxic Coordinates: Hard Cover Edition* (Elsevier, 2006).

Publisher's note Springer Nature remains neutral with regard to jurisdictional claims in published maps and institutional affiliations.

Open Access This article is licensed under a Creative Commons Attribution-NonCommercial-NoDerivatives 4.0 International

License, which permits any non-commercial use, sharing, distribution and reproduction in any medium or format, as long as you give appropriate credit to the original author(s) and the source, provide a link to the Creative Commons licence, and indicate if you modified the licensed material. You do not have permission under this licence to share adapted material derived from this article or parts of it. The images or other third party material in this article are included in the article's Creative Commons licence, unless indicated otherwise in a credit line to the material. If material is not included in the article's Creative Commons licence and your intended use is not permitted by statutory regulation or exceeds the permitted use, you will need to obtain permission directly from the copyright holder. To view a copy of this licence, visit <http://creativecommons.org/licenses/by-nc-nd/4.0/>.

© The Author(s) 2025

Methods

Materials

All chemicals and reagents were of the highest purity grade. Lipoid: hydrogenated soy phosphatidylcholine (HSPC) (catalogue number Lipoid S PC-3) and [*N*-(methoxypolyethyleneglycol-2000)-1,2-distearoyl-sn-glycero-3-phosphoethanolamine, sodium salt] (DSPE-PEG 2000) (catalogue number PE18:0/18:0, PEG 2000). Evonik: cholesterol (PhytoChol Inject HU). KetHCl injectable solution (100 mg ml⁻¹; Dechra Pharmaceuticals, procured through Stanford University Environmental Health & Safety). Hiemdia: ammonium sulfate (catalogue number PCT0003). Fisher Scientific: absolute ethanol (200 proof) (catalogue number BP2818-100), sucrose (catalogue number S5-500), HPLC and LC/MS grade water, methanol, acetonitrile, 2-propanol and formic acid. Sigma-Aldrich: HEPES buffer solution (catalogue number 83264-500ML-F) and L-histidine monohydrochloride monohydrate (catalogue number H8125). Repligen: TFF filters (C02-S05U-05-N (SN 20020493-03/21-057)). Lampire Biological Laboratories: male canine plasma (catalogue number 7302009). Cytiva: PD-10 column Sephadex G-25 M (catalogue number 17085101) and Sephacryl S-500 (catalogue number 1706130). Milli-Q water was used to prepare all buffers. Millipore Sigma: Cerilliant certified standard solutions of ketamine hydrochloride, ketamine-D₃ hydrochloride, norketamine hydrochloride, norketamine-D₄ hydrochloride and hydroxynorketamine hydrochloride; Supel BioSPME 96-Pin Devices (product number 59680-U).

AAL synthesis and characterization

Liposome production. Initially, large multilamellar vesicles were prepared by dissolving lipid components (HSPC/DSPE-PEG 2000/cholesterol 52.8:42.3:4.8 molar ratio) in heated ethanol and then diluting the mixture to 10% ethanol with 250 mM ammonium sulfate alone or with 5–10% (by weight) sucrose, 5% glucose or 73 mM NaCl depending on the experiment. The solution was extruded (Avestin LF-50 with 200 nm pore polycarbonate Whatman filter at 65–70 °C) ten times to generate unilamellar liposomes. Samples were processed with tangential flow filtration (5 × 5-fold dilution/reconcentration) against a buffer of 10 mM HEPES, 145 mM NaCl (pH 7.4) with 0%, 5% or 10% sucrose depending on the internal buffer osmolarity, to generate a transmembrane ammonium gradient. For loading, the drugs were added to 10-fold diluted liposome at final 1 mg ml⁻¹ concentration and heated to 55 °C for 1.5 h. To remove the unencapsulated drug, repeated TFF (4 × 5-fold dilution/reconcentration) was performed against a buffer of 10 mM histidine (pH 7.4) with 10% or 15% sucrose. Finally, the samples were sterilized using a 220 nm PVDF filter and stored at 4 °C.

Physicochemical characterization. The Z-average diameter, polydispersity index (PDI) and zeta potential of liposomes were measured by dynamic light scattering (DLS) with a Malvern Zetasizer Nano ZS90 (Malvern). Cryo-electron microscopy (cryo-EM) was used for structural analysis. Drug loading efficiency was measured by destructing the liposome using methanol followed by HPLC to quantify the total drug presented in the sample and reported as DL in mg ml⁻¹ concentration. For the free drug measurement, initially unencapsulated drug was separated from liposome using PD10 column followed by HPLC to quantify the percent free drug using the following formula: FD(%) = (drug in free fraction/sum of drug in free and liposome fractions) × 100 (method details in Supplementary Information).

In vitro ultrasonic drug uncaging. PCR tube containing liposomes (1:4 diluted in canine plasma) was placed in a custom 3D-printed holder held at the focus of a 250 kHz or 650 kHz hydrophone-calibrated FUS transducer and degassed water of either 25 °C or 37 °C was used for coupling. For the flow uncaging, the focal zone of a 250 kHz FUS transducer was aligned with tubing through which liposomes, diluted 30-fold with canine plasma, were flowed at a rate of 130 µl min⁻¹. An ultrasound (60 s, 25% duty cycle, 5 Hz pulse repetition frequency (PRF), varying

peak pressure) was applied and a total volume of 1 ml was collected after sonication for each condition. Liposomes after uncaging were separated from unencapsulated free drug by a homemade Sephacryl S-500 column, with PBS as the elution buffer, collecting the first 5.5 ml of elute as the liposome fraction and the next 8 ml as the unencapsulated drug fraction. Drug concentration in each elute was quantified by HPLC. The % drug uncaging was calculated using the following formula:

%Drug uncaging

$$= \left(\frac{\text{Drug in free fraction}}{\text{Sum of drug in free and liposomal fractions}} \right) \times 100\%$$

In vitro acoustic emissions recordings during sonication of an AAL and its internal buffer. To characterize acoustic emissions during ultrasonic uncaging, the magnitude of the received echo spectrum was measured using a flow chamber set-up. In brief, the focal zone of a 250 kHz FUS transducer was aligned with a tubing segment through which liposomes flowed at a constant rate of 130 µl min⁻¹. Ultrasound was delivered with a 0.1% duty cycle and a 1 Hz pulse repetition frequency, with peak pressures varying across experimental conditions. A hydrophone (ONDA) was positioned 2.5 cm from the tubing at a 90° angle relative to the transducer axis to capture acoustic backscatter during sonication. The echo signals were collected by PicoScope and subjected to fast Fourier transform analysis. The resulting spectra were plotted to assess the frequency-dependent magnitude of the acoustic emissions.

Speed of sound measurement. A clean 20-gallon fish tank was filled with deionized water and degassed overnight. A 650 kHz 30 mm aperture f1.0 FUS transducer (Sonic Concepts), a 35.6 cm long PVC cylinder with a 1.5 inch diameter, and a hydrophone were placed in a row underwater. Both devices were linked to an oscilloscope (Keysight Technologies) to view the time of flight between the transducer and the hydrophone. The PVC pipe was wrapped in an ultrasound-compatible plastic probe cover and sealed with O-rings to create a separate internal fluid compartment. First, the pipe was loaded with 37 °C deionized water, and the ultrasound pulse arrival time was used as a reference, along with the known speed of sound in deionized water at 37 °C, for subsequent measurements. Each buffer was sequentially loaded after heating, and the difference in pulse arrival time was recorded. A temperature measurement after each run confirmed minimal heat loss. The differences in pulse arrival time owing to different speeds within the length of the pipe were translated into speeds of sound of the various buffers. Finally, measurements of density at 37 °C were performed by weighing 10 ml of each buffer using a balance.

Animals. All animal experiments were carried out in accordance with the Stanford IACUC and Administrative Panel on Laboratory Animal Care (APLAC). Male Long–Evans rats (Charles River Laboratories; Envigo) and male Sprague–Dawley rats (Charles River Laboratories) were used in all in vivo studies with ketamine and ropivacaine, respectively. All rats were between 7 and 10 weeks old with body weight 250–450 g. Isoflurane was used to anaesthetized animals for surgical and terminal procedures and briefly for awake animal experimental set-up.

Animal treatment preparation. Ketamine hydrochloride (Dechra Veterinary Products) was diluted in 0.9% sterile saline to obtain 1 mg ml⁻¹ solutions. All treatments were administered via intravenous tail vein infusion continuously over 5 min with an infusion pump (World Precision Instruments).

In vivo ultrasound protocol and blood–brain barrier (BBB) opening verification. A custom 250 kHz FUS transducer (designed and constructed by R. Watkins, Stanford University) powered by an amplifier (240 L, E&I) was utilized in all in vivo experiments. Calibration of voltages

was conducted using a hydrophone (ONDA). Skull attenuation was accounted for and calculated based on weight⁴⁴ to achieve the desired in situ pressure. In all experiments where ultrasound was applied, continuous FUS was applied to either the mPFC or RsC after 2.5 min of drug infusion for 2.5 min (250 kHz, 25% duty cycle, 1.1 MPa estimated peak in situ pressure, 50 ms pulse width). For BBB opening verification, 4 ml kg⁻¹ of 2% Evans Blue dye was administered via the tail vein immediately after FUS treatment and ketamine-loaded liposome infusion. The rat was then anaesthetized and perfused with PBS before the brain was extracted. As a positive control for BBB opening, Definity microbubble infusion was used instead of ketamine-loaded liposomes, with ultrasound applied at 0.5 MPa with 1% duty cycle and 1 Hz PRF for 3 min.

Ultrasound simulations. To simulate the pressure-field distributions during FUS treatment, a male Long–Evans rat (weight 453 g) was imaged on a Quantum GX micro-CT. The obtained micro-CT image was 1,024 × 1,024 × 553 with a cubic voxel size of 0.086 mm. The images were resampled linearly to a cubic voxel size of 0.34 mm. The bone, soft tissue and water were isolated based on their Hounsfield units (1,200 HU for bone/soft tissue and 930 HU for soft tissue/water threshold). Density and sound speed were linearly interpolated in each region using hounsfield2density, a predefined function through the k-Wave MATLAB toolbox⁴⁵. The region surrounding the animal was defined as water. The transducer was defined as a bowl with a diameter and radius of curvature of 100 mm. At 250 kHz centre frequency, the points per wavelength was 17.44 in water and Courant–Friedrichs–Lewy stability criterion of 0.1 leading to a time step of 22.8 ns. The simulation was run for 85 μ s, allowing the initial wave to travel to the length of the simulation grid (125 mm).

In vivo measurements of temperature change with ultrasound.

To assess temperature changes during in vivo ultrasound-mediated drug uncaging, thermal measurements were taken adjacent to the skull at both the sonicated and contralateral brain sites. After dorsal scalp exposure, 2 mm burr holes were drilled into the skull to allow for insertion of a thermocouple probe. Animals underwent the in vivo ultrasound protocol listed above. Thermocouple probes were inserted 3 mm vertically into the brain parenchyma through the burr holes to measure temperature at three time points: immediately before ultrasound exposure, immediately after and 1 min post-exposure.

SPME. Rats were fixed into a stereotaxic frame, administered 2 ml of saline subcutaneously and kept on a heating pad at 37 °C. After dorsal scalp exposure, 2 mm burr holes were drilled into the skull for SPME pin insertion (relative to bregma, –5 mm A/P and ± 2.5 mm M/L for Fig. 4; +3.2 mm A/P for mPFC, or –4 mm for RsC, both at +1 mm M/L to the right). A durotomy was performed with a 32 g needle. Burr holes were used only in the SPME and thermal probe experiments to permit passage of the probes for direct assessment of the brain immediately after treatment. For rat subjects that received ultrasound, the ultrasound transducer was positioned directly above the desired burr hole via a three-axis positioning system (ThorLabs), with a coupling cone and ultrasound gel for coupling. Rats received 1.5 mg kg⁻¹ of SonoKet, KetHCl or saline vehicle. Pins were loaded into a custom-designed, 3D-printed stereotaxic holder for precise positioning and sampling, inserted 3 mm ventrally into the brain via the burr holes (SPME absorptive medium centred at –2.5 mm ventral) and left in contact with the rat brain tissue for 5 min (refs. 46–49). Post-sampling, SPME pins were washed to remove residual blood, desorbed into 50 μ l of MeOH/H₂O (9:1 v/v) solvent containing 1% formic acid and quantified by liquid chromatography-mass spectrometry/mass spectrometry (LC-MS/MS; method details in Supplementary Information).

Blood pharmacokinetics. Blood samples from rats ($n = 3$ per group) that received 1.5 mg kg⁻¹ intravenous bolus or infused SonoKet or dose-matched KetHCl were collected via tail snipping into EDTA at

different time points, and 3–4× cold acetonitrile was mixed to precipitate the plasma protein, which was then removed using a centrifuge. The collected supernatant was dried, reconstituted with 100 μ l of MeOH/H₂O (9:1 v/v) solvent containing 1% formic acid and quantified by LC-MS/MS.

Biodistribution. Adult rats ($n = 4$ per group) received either free or liposomal ketamine as an intravenous bolus dose of 1.5 mg kg⁻¹. Rats were killed at 1 h from the time of administration and perfused with 1× PBS via transcardial perfusion to remove blood from the systemic circulation. The collected brain, liver, kidney, spleen, lung, heart and spinal cord were homogenized in equal-weight volume of 1× PBS. Similar to blood processing, 3–4× cold acetonitrile was mixed to precipitate the protein, which was then removed using a centrifuge. The collected supernatant was dried, reconstituted with 100 μ l of MeOH/H₂O (9:1 v/v) solvent containing 1% formic acid and quantified by LC-MS/MS.

Awake-restraint electrophysiology recording and analysis

Surgical set-up. Animals were anaesthetized and positioned stereotaxically for implantation of custom ECoG electrodes. A midline incision was made over the scalp and five holes were drilled through the skull with stereotaxic guidance⁴³. All electrodes were positioned relative to bregma. mPFC electrodes were positioned at +1 mm A/P and +2 mm M/L to the right (positive electrode), and –6 mm A/P and ± 2 mm M/L (ground and reference electrodes, respectively). To provide enough ultrasound clearance without sonicating the electrodes in experiments where the RsC was sonicated while recording from the mPFC, the ground and reference electrodes were both moved to –11 mm A/P and respectively ± 2 mm M/L. Two stabilizing screws were implanted at –2 mm A/P and ± 3 mm M/L for structural integrity. RsC electrodes for all recordings from the RsC were positioned at –5 mm A/P and +3 mm M/L to the right (positive electrode), and –11 mm A/P and ± 3 mm M/L (ground and reference electrodes, respectively). Two stabilizing screws were implanted at –8 mm A/P and ± 4 mm M/L for structural integrity. Electrodes were screwed into the skull without breaching the dura and dental cement applied to fix the electrodes in place. Animals were housed in separate cages afterwards and allowed for at least 7 days of recovery before recordings.

ECoG recording. At the beginning of each recording session, rats were briefly anaesthetized to be catheterized via the tail vein, placed in a thin, flexible plastic restraint cone (Amazon.com), and positioned in a custom head-restraining apparatus⁵⁰. Rats received oxygen via the nose cone to prevent hypoxia. Recordings were performed with an 8-Channel Cyton Biosensing Board^{51,52} at a sampling frequency of 1,000 Hz. For subjects that received ultrasound, the transducer was positioned directly above either the mPFC (+3.2 mm A/P, –0.5 mm M/L) or the RsC (–4 mm A/P, 0 mm M/L) via the 3-axis positioning system and coupled with ultrasound gel. Implanted screws were utilized for precise targeting according to the rat brain atlas⁴³. Data acquisition began 25–30 min after the animal is in the restraint to allow for complete isoflurane clearance. A baseline acquisition (5 min) was recorded before starting the treatment. Rats received 0.75 mg kg⁻¹ of SonoKet, KetHCl or saline vehicle. Data were acquired continuously for 35 min following a 5 min baseline and a 5 min treatment infusion protocol, for a total recording of 45 min.

Data analysis. Electrophysiological data were filtered using MNE-Python with a band-pass filter with a low cut-off of 1 Hz and a high cut-off of 200 Hz (ref. 53). The data were then denoised by decomposing into 5 levels of Daubechies 8 wavelets, zeroing outlier coefficients and then reconstructing the modified data⁵⁴. The first 45 min of the recording was defined as a single epoch and time–frequency representation was computed with a multitaper technique and adjusted to baseline (initial 0–5 min of recording) with percent change from baseline using MNE-Python. For band power trace plots, the time–frequency representation was averaged within frequency band cut-offs (delta, 1–4 Hz;

theta, 4–8 Hz; alpha, 8–15 Hz; beta, 15–25 Hz; gamma, 25–55 Hz) and a moving average of the band power was computed with a 2-min-long convolving window²⁷. One recording within the RsC 1 mg kg⁻¹ KetHCl condition was excluded owing to excessive artefacts that could not be corrected by denoising. The area under the curve (AUC) was calculated by integrating the percent of power change within each frequency band as indicated above in time bins indicated as time of sonication (7.5–10 min), time immediately after treatment (10–25 min) and time after clearance (25–45 min) and depicted in arbitrary units.

Behavioural open-field analysis

Rats were surgically implanted with a targeting screw and given at least 7 days to recover before behavioural tests. To acclimate to the experimenter and reduce stress, rats were handled 3 days before recording. All behavioural tests were performed in an environmentally controlled room. Open-field locomotor activity was recorded from above in a custom-built white Plexiglas apparatus (90 cm × 90 cm × 40 cm). Animals were placed at the centre of the field and randomized for the treatment group.

Rats were placed under isoflurane briefly to be catheterized via the tail vein and loaded into the awake restraint⁵⁰. They were administered oxygen via the nose cone within the restraint to prevent hypoxia. After ensuring that the rats are fully awake before starting treatment, rats received an intravenous infusion of 0.75 mg kg⁻¹ SonoKet, KetHCl or saline vehicle for 5 min, followed by the in vivo ultrasound protocol. After treatment, rats were immediately placed at the centre of the arena, where they were allowed to freely explore for 20 min while locomotor activity was recorded.

Before analysis, videos were first reencoded for format compatibility and clipped to 20 min starting at 5 s after the initialization of the recording with FFmpeg. ToxTrac was then used to track animal position with tracking settings matching the ToxId algorithm and detection settings adjusted ad hoc^{55,56}. Custom Python scripts were then used to quantify and plot cumulative frame-to-frame distance travelled and time spent in the centre of the open field, which was defined as a concentric square field with half the width of the full square field.

Ropivacaine in vivo experiments

Mechanical sensitivity. Rats were acclimated to a raised stainless steel mesh table for 30 min. Baseline paw withdrawal responses were obtained using monofilaments and the von Frey percent response method (10 pokes per filament 1–26 g)^{57,58}. On the basis of baseline responses, the 26 g monofilament was selected to evaluate the effects of local uncaging ropivacaine. On the procedure day, rats were anaesthetized during the experiment. Saline vehicle or ropivacaine-loaded liposomes were administered, followed by application of ultrasound using a dorsal approach to target the sciatic nerve. Paw withdrawal response was then evaluated using the 26 g monofilament and the von Frey percent response method 30 min, 1 h and 4 h post-treatment.

Electrocardiographic analysis. Under anaesthesia, three alligator electrodes were placed on the rats in limb lead II position: the negative electrode was placed on the front paws and the positive electrode on the left hind paw. ECG recordings were taken at baseline, immediately and 5 min after injection of either free ropivacaine-HCl or ropivacaine-loaded AAL using a Sy-WO2 Vet 3 Channel ECG Machine (Sunny Medical Equipment Limited). The following changes in the ECG pattern were assayed: heart rate (bpm), duration of QRS complex and QT interval (corrected for given heart rate in each animal), and periodic repolarization dynamics (PRD).

Histological safety analysis

Drug administration and tissue collection. Rats were administered an intravenous infusion of 0.75 mg kg⁻¹ SonoKet, dose-matched KetHCl or vehicle over 5 min ($n = 3$ per group), followed by ultrasound application (−5 mm A/P and +2.5 mm M/L to the right relative to bregma). After

72 h post-treatment, the animals were anaesthetized and transcardially perfused with 1× PBS followed by 4% paraformaldehyde (PFA) diluted in PBS. Brains were extracted and stored in 4% PFA for 24 h, 15% sucrose for the next 48 h and 30% sucrose for the last 48 h. They were washed in PBS and frozen in embedding medium. Coronal brain sections (30 µm thick) were cut using a CM1800 cryostat (Leica Microsystems) and were stored in 30% sucrose and 30% ethylene glycol in 0.1 MPB at −20 °C until processed for immunohistochemistry.

Microscopy and image analysis. Every 12th section (360 µm apart) was stained with haematoxylin and eosin (H&E; Vector Laboratories), Fluoro-Jade C (Biosensis), recombinant anti-GFAP antibody (ab33922, Abcam) and recombinant IBA-1 (ab178846, Abcam) to evaluate for parenchymal damage, neuronal degeneration, and astrocytic or microglial activation, respectively. Alexa Fluor 488 secondary antibody (Thermo Fisher Scientific) was used after primary anti-GFAP incubation. Cy5 secondary antibody (Thermo Fisher Scientific) was used after primary anti-IBA1 incubation. Tissue sections were free-float mounted on microscope glass slides (Fisher). All histology images were collected with a fluorescence microscope (BZ-X800, Keyence). For quantifiable histological markers (Fluoro-Jade C, IBA-1⁺ and GFAP⁺ cells), signals above thresholded background were used for manual region of interest segmentation to calculate the total mean fluorescent area of cells using BZ-X Advanced Analysis Software (Keyence). For the ropivacaine uncaging safety analysis, a similar process was complete except for targeting and collecting of the sciatic nerve and surrounding thigh tissues following ropivacaine-HCl ($n = 3$) or ropivacaine-loaded AAL ($n = 3$) administration. Muscle and nerve tissues beneath the targeted site were extracted and stored in 4% PFA for 24 h. Tissues were frozen in optimal cutting medium compound and stored at −80 °C until serially sectioned with a cryostat at 7 µm. Every 20th section (140 µm apart) was stained with H&E for gross examination of tissue damage.

General statistical analysis

Rats were randomly assigned to treatment conditions. Data where $n \leq 4$ were plotted as bar plots and $n \geq 5$ were plotted as box plots. For comparisons between two groups, a two-tailed, two-sample Student's t -test was conducted. For comparisons between multiple groups, a one-way, two-sided, analysis of variance (ANOVA) was conducted, followed by a post hoc Tukey's honestly significant difference (HSD) test for pairwise comparisons. Effect size was calculated using Hedges g . All comparisons were two-tailed. Statistical tests, sample sizes N , corrected P values and effect sizes g are reported for each analysis in the text and figure captions. Pharmacokinetic parameters were estimated using the NonCompartment package⁵⁹ and comparisons were made with two-tailed Student's t -tests in R version 4.1.3. The remaining statistical analyses were performed using GraphPad Prism 10 (GraphPad Software) and custom scripts in Python.

Reporting summary

Further information on research design is available in the Nature Portfolio Reporting Summary linked to this article.

Data availability

Raw data underlying all figures and the code used to analyse the data are available via our GitHub repository at <https://github.com/Airan-Lab> (ref. 60). Any additional data not presented are available from the corresponding author upon reasonable request. Source data are provided with this paper.

References

- O'Reilly, M. A., Muller, A. & Hynynen, K. Ultrasound insertion loss of rat parietal bone appears to be proportional to animal mass at submegahertz frequencies. *Ultrasound Med. Biol.* **37**, 1930–1937 (2011).

45. Treeby, B. E. & Cox, B. T. k-Wave: MATLAB toolbox for the simulation and reconstruction of photoacoustic wave fields. *J. Biomed. Opt.* **15**, 021314 (2010).
46. Roy, K. S. et al. Optimizing a high-throughput solid-phase microextraction system to determine the plasma protein binding of drugs in human plasma. *Anal. Chem.* **93**, 11061–11065 (2021).
47. Huq, M., Tascon, M., Nazdrajic, E., Roszkowska, A. & Pawliszyn, J. Measurement of free drug concentration from biological tissue by solid-phase microextraction: in silico and experimental study. *Anal. Chem.* **91**, 7719–7728 (2019).
48. Hassani, S. A. et al. Dose-dependent dissociation of pro-cognitive effects of donepezil on attention and cognitive flexibility in rhesus monkeys. *Biol. Psychiatry Glob. Open Sci.* **3**, 68–77 (2023).
49. Boyacı, E. et al. High-throughput analysis using non-depletive SPME: challenges and applications to the determination of free and total concentrations in small sample volumes. *Sci. Rep.* **8**, 1167 (2018).
50. Stenroos, P. et al. Awake rat brain functional magnetic resonance imaging using standard radio frequency coils and a 3D printed restraint kit. *Front. Neurosci.* **12**, 548 (2018).
51. OpenBCI Software. OpenBCI. <https://openbci.com/> (2024).
52. OpenBCI_Python. OpenBCI Archive (2024); https://github.com/openbci-archive/OpenBCI_Python
53. Gramfort, A. et al. MEG and EEG data analysis with MNE-Python. *Front. Neurosci.* **7**, 267 (2013).
54. Welch, P. The use of fast Fourier transform for the estimation of power spectra: a method based on time averaging over short, modified periodograms. *IEEE Trans. Audio Electroacoustics* **15**, 70–73 (1967).
55. Rodriguez, A., Zhang, H., Klaminder, J., Brodin, T. & Andersson, M. ToxId: an efficient algorithm to solve occlusions when tracking multiple animals. *Sci. Rep.* **7**, 14774 (2017).
56. Rodriguez, A. et al. ToxTrac: a fast and robust software for tracking organisms. *Methods Ecol. Evol.* **9**, 460–464 (2018).
57. Deuis, J. R., Dvorakova, L. S. & Vetter, I. Methods used to evaluate pain behaviors in rodents. *Front. Mol. Neurosci.* **10**, 284 (2017).
58. Kolarczyk, L. M. & Williams, B. A. Transient heat hyperalgesia during resolution of ropivacaine sciatic nerve block in the rat. *Reg. Anesth. Pain Med.* **36**, 220–224 (2011).
59. Kim, H., Han, S., Cho, Y.-S., Yoon, S.-K. & Bae, K.-S. Development of R packages: ‘NonCompart’ and ‘ncar’ for noncompartmental analysis (NCA). *Transl. Clin. Pharmacol.* **26**, 10 (2018).
60. Airan, R. D. et al. Purohitetal. *GitHub* <https://github.com/Airan-Lab> (2025).

Acknowledgements

We would like to thank P. Purdon, B. Heifets, C. Rodriguez, N. Williams, A. Schatzberg, M. Michaelides, R. Malenka, W. T. Newsome, B. Knutson, V. Tawfik, K. Butts Pauly and K. Ferrara for a variety of useful discussions guiding the study design and analysis. We would like to thank S. Lendor and J. Pawliszyn for guidance regarding solid-phase microextraction. We would like to thank R. Watkins for guidance and support for producing the ultrasound hardware utilized in these experiments. We would also like to thank the Stanford CryoEM Center (cEMc), including E. Montabana and B. Singal, for technical assistance in cryo-EM imaging. We would like to thank the whole Airan Lab and its alumni for helpful discussions.

Author contributions

Conceptualization: R.D.A., Y.X., M.P.P., B.J.Y. and K.S.R. Methodology: M.P.P., B.J.Y., K.S.R., Y.X., S.N.E., M.M.A., J.B.W., A.R.H., P.J.M. and R.D.A. Investigation: M.P.P., B.J.Y., K.S.R., Y.X., S.N.E., M.M.A., A.R.H., G.P.B.M., P.J.M., A.K.T., E.M., N.M., A.K.K. and D.G.L. Analysis: K.S.R., B.J.Y., Y.X., S.N.E., P.J.M., M.P.P., M.M.A., A.R.H., G.P.B.M. and R.D.A. Visualization: M.P.P., B.J.Y. and R.D.A. Funding acquisition: R.D.A. Project administration: R.D.A. Supervision: R.D.A. Writing (initial draft): B.J.Y., M.P.P. and R.D.A. Review and editing: all authors.

Competing interests

R.D.A. has equity or has received consulting fees from Cordance Medical, NaviFUS and Lumos Labs and grant funding from AbbVie Inc. All other authors declare no competing interests.

Additional information

Extended data is available for this paper at

<https://doi.org/10.1038/s41565-025-01990-5>.

Supplementary information The online version contains supplementary material available at <https://doi.org/10.1038/s41565-025-01990-5>.

Correspondence and requests for materials should be addressed to Raag D. Airan.

Peer review information *Nature Nanotechnology* thanks the anonymous reviewers for their contribution to the peer review of this work.

Reprints and permissions information is available at www.nature.com/reprints.

Extended Data Table 1 | Typical physicochemical characterization of the presented drug-loaded liposomes

Formulation	Average Size (nm)	PDI	Zeta Potential (mV)	Drug Loading (mg/mL)	Free Drug (%)	Entrapment Efficiency (%)	pKa	LogP
Ketamine Liposome (KL)							7.5	2.2
KL	164.07 ± 6.5	0.06 ± 0.02	-45.2	3.19 ± 0.17	4.96 ± 0.80	24-27		
S5-KL a.k.a. SonoKet	158.06 ± 5.5	0.08 ± 0.01	-46.3	3.41 ± 0.24	3.09 ± 1.38	25-29		
S10-KL	160.86 ± 6.0	0.06 ± 0.03	-44.9	3.27 ± 0.21	3.59 ± 2.02	25-28		
NaCl5-KL	160.36 ± 7.0	0.06 ± 0.02	-48.7	3.21 ± 0.14	4.62 ± 2.16	25-27		
Glu5-KL	157.86 ± 7.0	0.09 ± 0.01	-47.7	3.24 ± 0.20	3.24 ± 2.42	24-28		
Lidocaine Liposome (LL)							8.0	2.3
LL	159.90 ± 2.5	0.06 ± 0.01	-49.5	4.61 ± 0.07	1.82 ± 0.32	36-39		
S5-LL	161.10 ± 2.1	0.06 ± 0.02	-49.1	4.50 ± 0.14	1.45 ± 0.45	36-40		
Bupivacaine Liposome (BL)							8.1	3.4
BL	165.80 ± 3.2	0.09 ± 0.01	-55.4	5.60 ± 0.09	3.86 ± 1.02	39-42		
S5-BL	164.38 ± 3.6	0.06 ± 0.03	-49.2	5.81 ± 0.12	4.02 ± 3.02	39-44		
Ropivacaine Liposome (RL)							8.1	2.9
RL	169.73 ± 3.2	0.07 ± 0.02	-43.3	4.32 ± 0.35	3.81 ± 2.12	38-43		
S5-RL a.k.a. SonoRopi	166.71 ± 3.8	0.08 ± 0.01	-49.2	4.51 ± 0.42	4.85 ± 1.07	37-41		

Note: S5=5% additional sucrose, S10=10% additional sucrose in the internal buffer of the liposome. The pKa and logP values were derived from PubChem and DrugBank.

Extended Data Table 2 | Measured acoustic parameters and osmolarity of plasma and the varied liposome internal and external media

Buffers	Density ρ (Kg/m ³) ^a	Speed of Sound c (m/s) ^a	Acoustic Impedance $Z = \rho c$ (MPa-s/m)	Bulk Modulus $K = \rho c^2$ (MPa)	Osmolarity (mOsm)
External medium during uncaging					
Plasma	1026.6	1519.42	1.55983	2370.05	313-317
Storage Buffer					
10 mM Histidine, pH 7.4 + 10% Sucrose	1040.1	1528.55	1.58984	2430.16	379-383
Liposome internal medium					
250 mM Ammonium Sulfate	1018.5	1527.90	1.55616	2377.67	534-537
250 mM Ammonium Sulfate + 5% (146 mM) Sucrose	1038.2	1543.13	1.60207	2472.21	670-671
250 mM Ammonium Sulfate + 10% Sucrose	1054.3	1564.15	1.64908	2579.41	817-822
250 mM Ammonium Sulfate + 73 mM NaCl	1020.4	1533.80	1.56508	2400.53	646-647
250 mM Ammonium Sulfate + 146 mM Glucose	1032.3	1544.47	1.59435	2462.44	663-666

^a The density and speed of sound measurements demonstrate a relative error below 0.002.

Extended Data Table 3 | Pharmacokinetic analysis of ketamine and its metabolites following ketamine-loaded AAL or free ketamine 1.5 mg/kg bolus intravenous administration

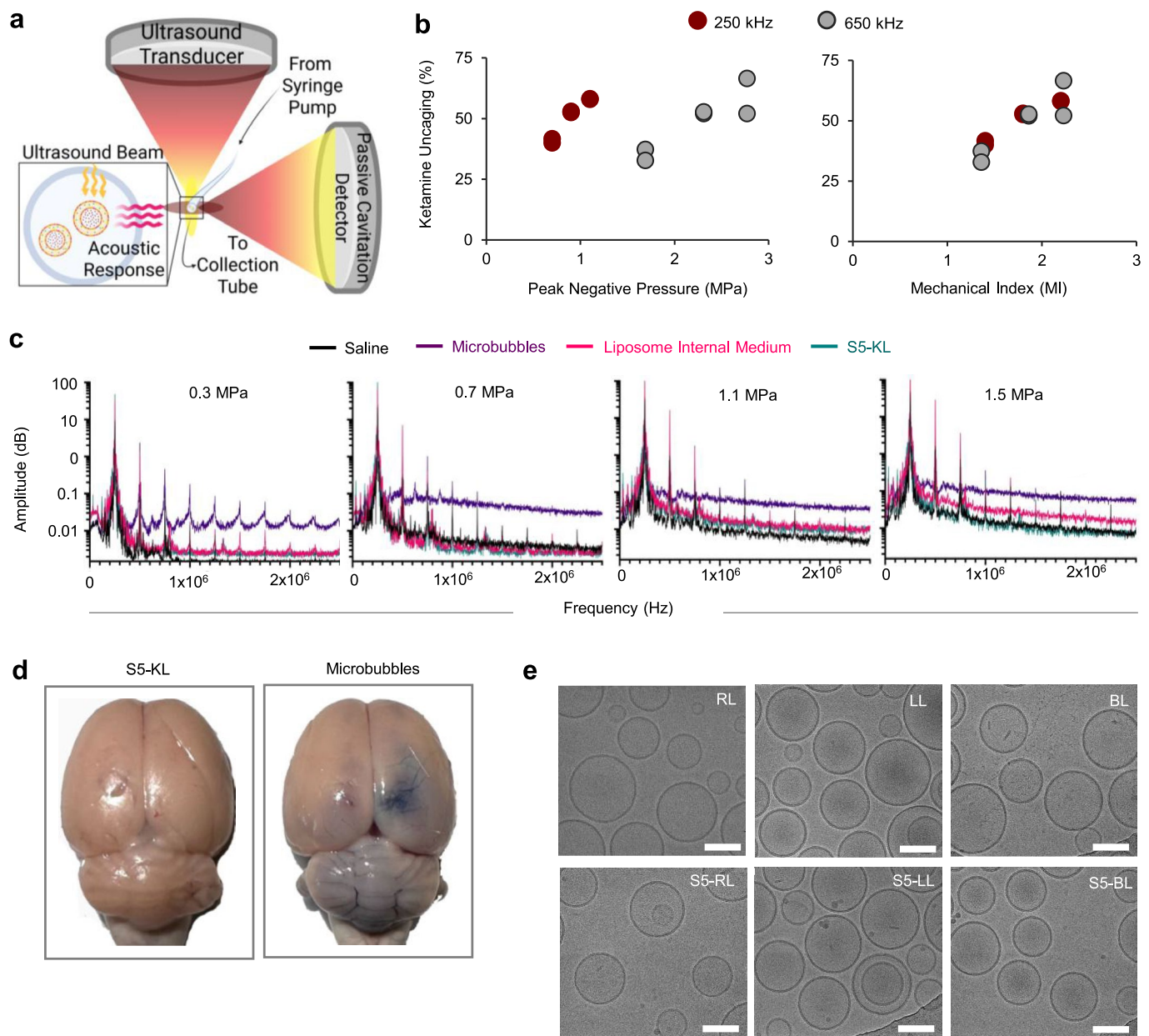
	Units	Ketamine AAL (Mean \pm SD)	Free Ketamine (Mean \pm SD)	P-value AAL vs Free Ketamine
Ketamine				
C_{\max}	ng/mL	2043.35 \pm 203.59	789.20 \pm 140.32	** 0.001
T_{\max}	m	1 \pm 0	1 \pm 0	NA
C_0	ng/mL	4708.81 \pm 720.06	1074.98 \pm 138.67	* 0.010
$t_{1/2}$	m	11.22 \pm 2.52	8.82 \pm 1.07	0.236
AUC_{0-t}	ng/mL m	9269.64 \pm 1023.11	6357.64 \pm 1155.59	* 0.031
$AUC_{0-\infty}$	ng/mL m	10977.88 \pm 703.92	7819.91 \pm 1162.77	* 0.023
MRT_{0-t}	m	4.04 \pm 0.03	6.83 \pm 0.09	*** 0.0001
$MRT_{0-\infty}$	m	9.19 \pm 1.82	11.78 \pm 1.16	0.118
VZ	L	0.52 \pm 0.16	0.58 \pm 0.12	0.68
Cl	L/m	0.032 \pm 0.0025	0.045 \pm 0.0038	* 0.011
VSS	L	0.30 \pm 0.08	0.53 \pm 0.093	* 0.031
Norketamine				
C_{\max}	ng/mL	328.50 \pm 8.24	58.87 \pm 4.35	*** 0.00001
T_{\max}	m	1 \pm 0	11.67 \pm 7.64	0.136
C_0	ng/mL	413.68 \pm 37.18	31.21 \pm 8.11	** 0.002
AUC_{0-t}	ng/mL m	3271.82 \pm 148.01	968.99 \pm 93.43	*** 0.00008
MRT_{0-t}	m	7.94 \pm 0.38	10.44 \pm 0.30	** 0.001
Hydroxynorketamine				
C_{\max}	ng/mL	362.06 \pm 37.21	128.06 \pm 6.58	** 0.006
T_{\max}	m	2.83 \pm 2.02	16.67 \pm 5.77	* 0.041
C_0	ng/mL	343.63 \pm 60.90	28.30 \pm 5.38	* 0.011
AUC_{0-t}	ng/mL m	5548.76 \pm 723.45	2045.42 \pm 130.49	* 0.011
MRT_{0-t}	m	9.40 \pm 0.16	10.89 \pm 0.42	* 0.015

C_{\max} : maximum concentration; T_{\max} : time of maximum concentration; C_0 : concentration extrapolated to t0; $t_{1/2}$: half life; AUC_{0-t} : area under the curve from 0 to last time point; $AUC_{0-\infty}$: area under the curve from 0 to infinity; MRT_{0-t} : mean residence time from 0 to last time point; $MRT_{0-\infty}$: mean residence time from 0 to infinity; VZ: volume of distribution; Cl: clearance; VSS: volume of distribution at steady state; *: $p < 0.05$; **: $p < 0.01$; ***: $p < 0.001$.

Extended Data Table 4 | Pharmacokinetic analysis of ketamine and its metabolites following ketamine-loaded AAL or free ketamine 1.5 mg/kg over 5 min intravenous infusion

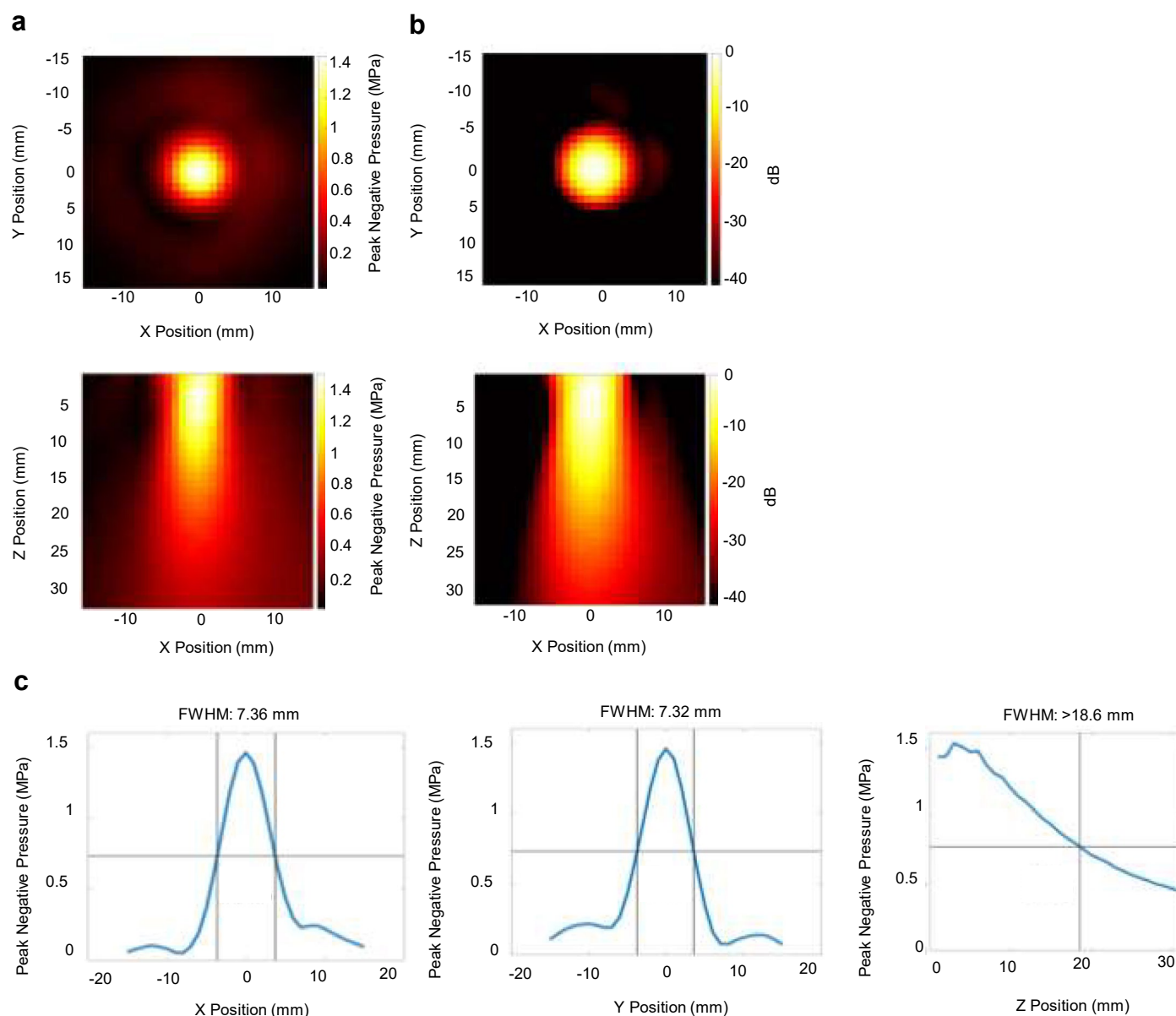
	Units	Ketamine AAL (Mean \pm SD)	Free Ketamine (Mean \pm SD)	P-value AAL vs Free Ketamine
Ketamine				
C_{\max}	ng/mL	381.60 \pm 56.44	270.16 \pm 38.97	0.164
T_{\max}	m	5 \pm 0	5 \pm 0	NA
$t_{1/2}$	m	16.33 \pm 0.99	17.00 \pm 3.97	0.851
AUC_{0-t}	ng/mL m	4416.27 \pm 592.34	4098.46 \pm 246.48	0.585
$AUC_{0-\infty}$ (obs)	ng/mL m	6847.83 \pm 13.09.70	7116.36 \pm 1027.23	0.842
MRT_{0-t}	m	8.29 \pm 0.05	9.47 \pm 0.26	0.089
$MRT_{0-\infty}$ (obs)	m	21.14 \pm 1.23	24.56 \pm 5.65	0.544
VZ (obs)	L	1.25 \pm 0.10	1.37 \pm 0.33	0.700
Cl	L/m	0.053 \pm 0.007	0.056 \pm 0.001	0.713
VSS (obs)	L	1.143 \pm 0.059	1.42 \pm 0.406	0.510
Norketamine				
C_{\max}	ng/mL	141.59 \pm 19.37	106.76 \pm 9.82	0.078
T_{\max}	m	5 \pm 0	15 \pm 14.14	0.500
$t_{1/2}$	m	28.33 \pm 6.66	NA	NA
AUC_{0-t}	ng/mL m	2365.84 \pm 188.01	1898.10 \pm 2.51	0.127
MRT_{0-t}	m	9.98 \pm 0.41	10.83 \pm 1.16	0.482

Hydroxynorketamine levels were too low for the pharmacokinetics model to converge C_{\max} : maximum observed concentration; T_{\max} : time of maximum observed concentration; $t_{1/2}$: half life ($\ln(2) / \lambda_Z$); AUC_{0-t} : area under the curve from 0 to last time point; $AUC_{0-\infty}$ (obs): area under the curve from 0 to infinity observed; MRT_{0-t} : mean residence time from 0 to last time point; $MRT_{0-\infty}$ (obs): mean residence time from 0 to infinity observed; VZ (obs): volume of distribution observed; Cl: clearance observed; VSS (obs): volume of distribution at steady state observed.

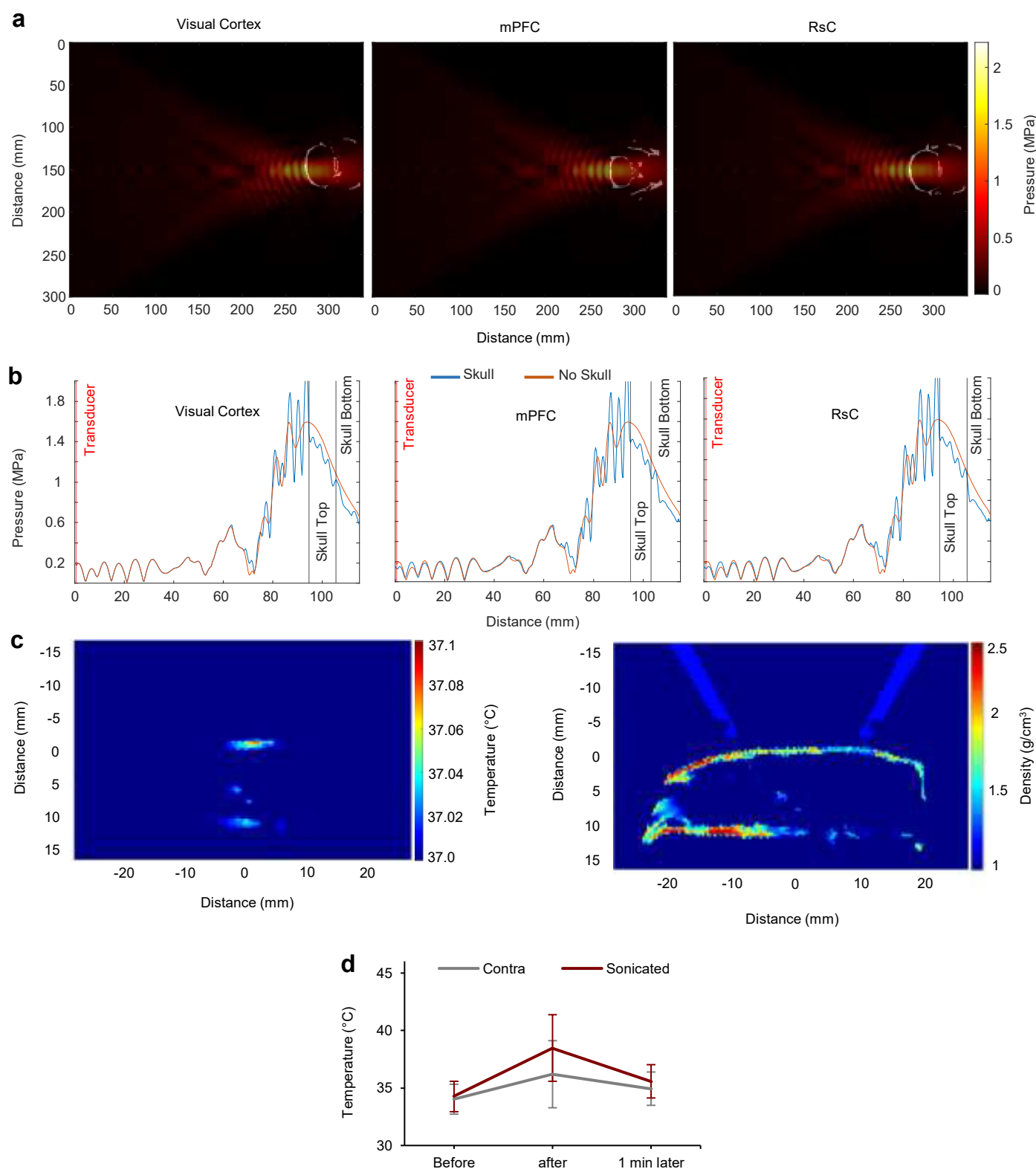


Extended Data Fig. 1 | Acoustic characterization of uncaging and in vivo assessment of cavitation risk. a. Schematic of flow chamber with thin-walled silicone tubing (0.1 mm wall thickness, 18 gauge) submerged in a large temperature controlled degassed water bath kept at 37 °C. The focal zone of the focused ultrasound transducer was placed on the tubing and a hydrophone placed at 2.5 cm from the tubing, with 90° between the hydrophone and the transducer, recording acoustic backscatter and emissions during sonication of infusion of one of four media: degassed saline (dilution medium used in vitro experiments), the liposome internal medium (250 mM $\text{NH}_4(\text{SO}_4)_2$ + 5% sucrose), the S5-KL = SonoKet liposomes diluted in saline to its estimated in vivo circulating concentration based on the observed in vivo ketamine blood concentrations ($\sim 10^9$ /mL particle concentration) and commercial microbubbles diluted to its estimated in vivo circulating concentration during blood-brain barrier opening experiments ($\sim 10^8$ /mL particle concentration). (<https://biorender.com/i9qghda>) **b.** Ketamine uncaging with 250 or 650 kHz sonication. Peak negative pressures of 0.7–1.1 MPa and 1.7–2.8 MPa for 250 and 650 kHz respectively (left), providing matching mechanical indices of 1.4–2.2 (right). Dotted line: drug release without

FUS in this apparatus. Data presented as mean and individual data points ($n = 2$). **c.** Received echo spectral magnitude following sonication of saline (Black), gas-filled microbubbles (Purple), liposome internal medium (Pink), or liposomes (S5-KL; Teal) versus frequency with 0.3, 0.9, 1.1 and 1.5 MPa in situ peak negative pressure, 250 kHz center frequency, 1 ms duration. **d.** To assess in vivo cavitation effects, S5-KL or commercial microbubbles were co-administered i.v. with Evans Blue dye and FUS was applied transcranially to the posterior right cortex of rats (center frequency 250 kHz, peak negative pressure of 1.1 MPa and 25% duty cycle for S5-KL, peak negative pressure of 0.5 MPa and 1% duty cycle for microbubbles). Brain dye extravasation was readily observed with microbubbles, indicating in vivo blood-brain barrier opening due to cavitation, with no such dye extravasation noted with S5-KL under gross or microscopic analysis of tissue sections, indicating no observable bioeffects of potential cavitation with S5-KL under these conditions. **e.** Representative TEM images of different API loaded liposomes show spherical morphology, with a liquid core with no observable gas or voids. (Scale Bar = 100 nm).

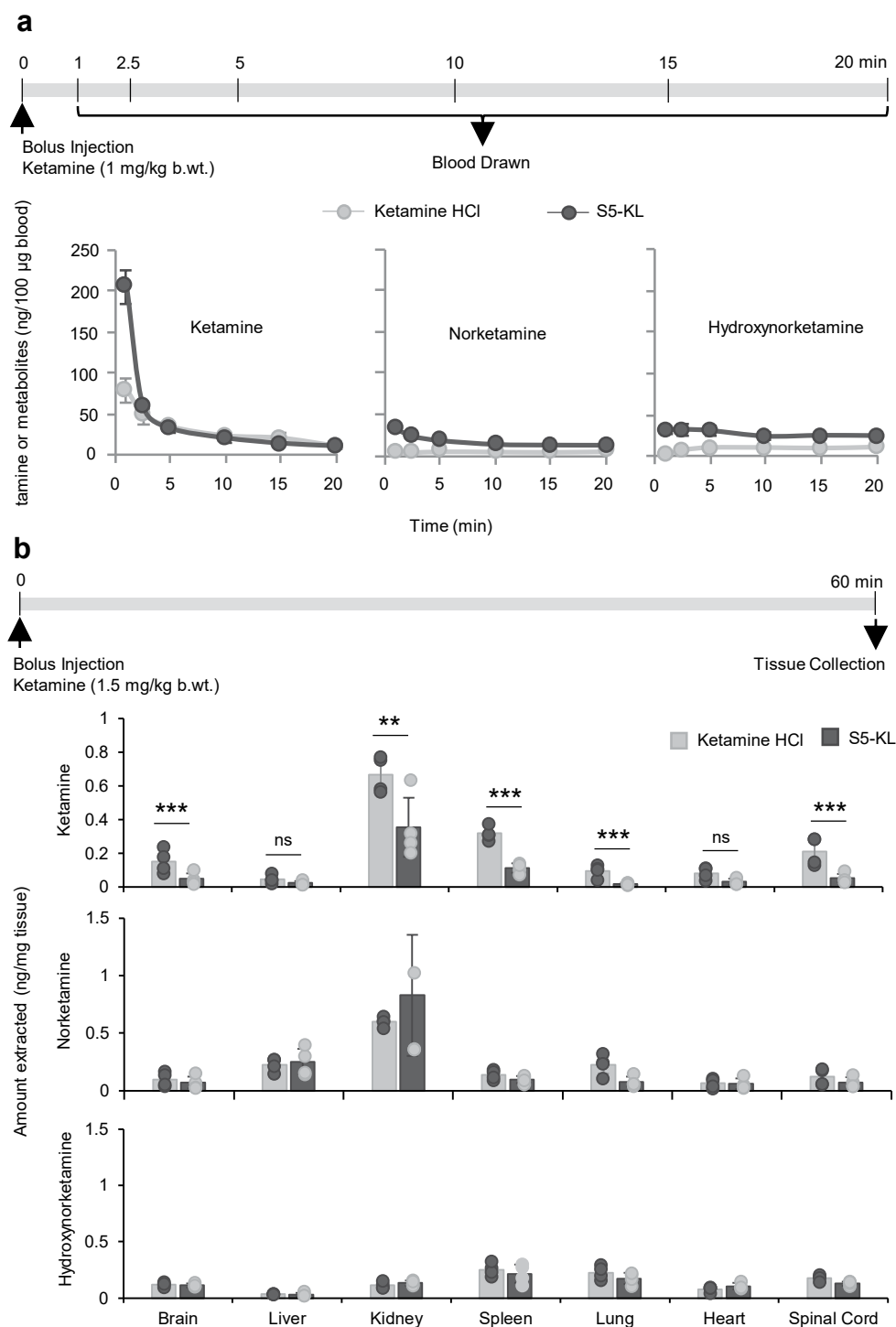


Extended Data Fig. 2 | Ultrasound transducer beam maps. Beam maps (**a**. in MPa, **b**. in dB) and **c**. 1D plots in the axial and lateral directions.



Extended Data Fig. 3 | Simulations of applied focused ultrasound with skull attenuation and its effect on temperature at sonicated site. a. Heatmap of beamform simulations overlaid on rat skull. **b.** Simulated pressure fields along the center of the field with and without intact rat skull with the top and bottom of the skull indicated. **c.** Left: Temperature change in the sagittal plane centered on the geometric focus simulated with k-wave. The expected temperature change is calculated after a 50 ms burst of ultrasound and 150 ms cooling time. Right:

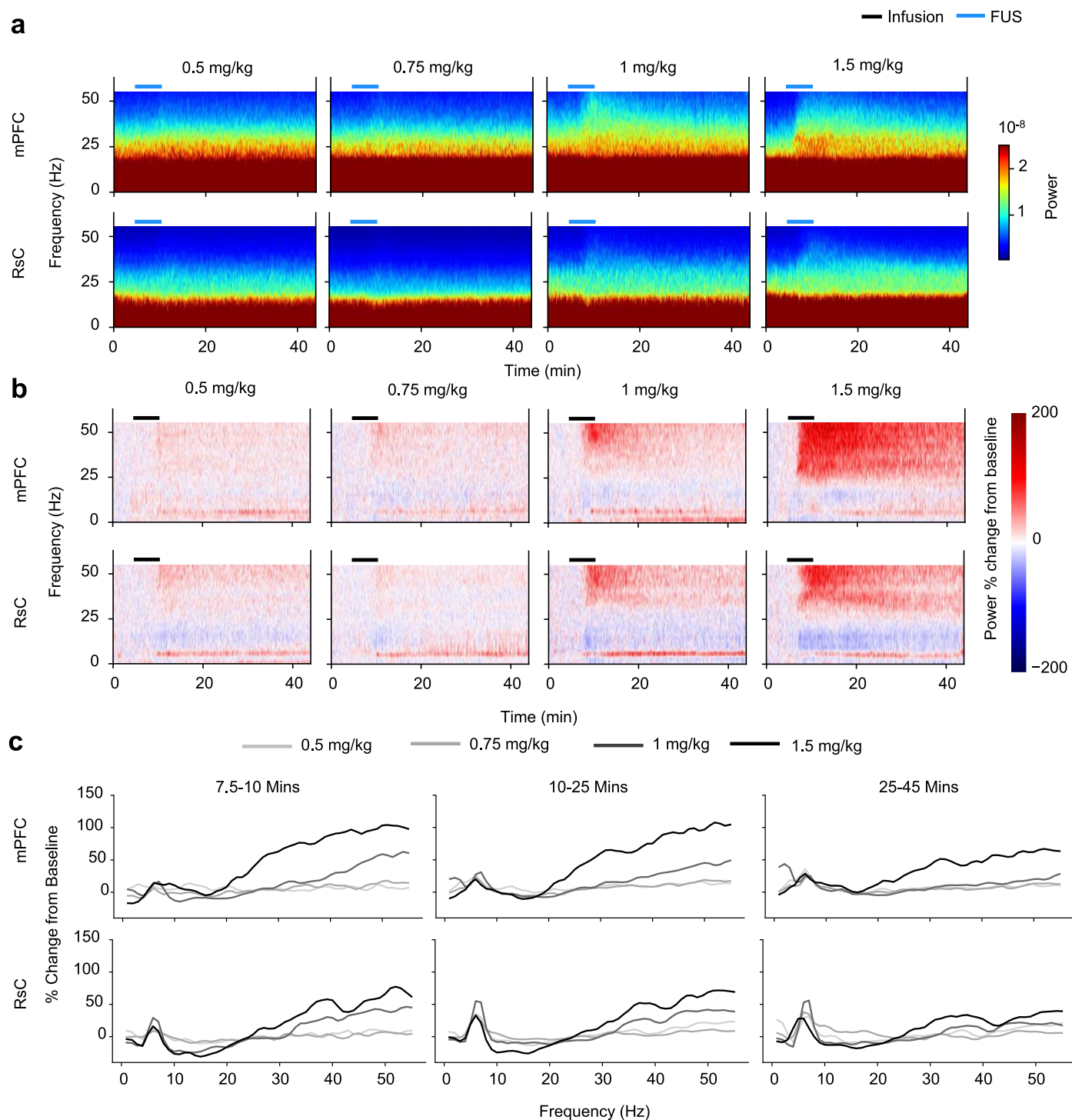
Density map of the same field of view in the k-wave simulation illustrating the orientation of the skull and coupling cone. The regions demonstrating heating with the ultrasound protocol correspond to bony or air interfaces of the rat head. **d.** Temperature change before, immediately after, and 1 minute after ultrasound exposure intracranially adjacent to the skull with the parameters used in the reported *in vivo* brain experiments.



Extended Data Fig. 4 | In vivo AAL pharmacokinetics and biodistribution.

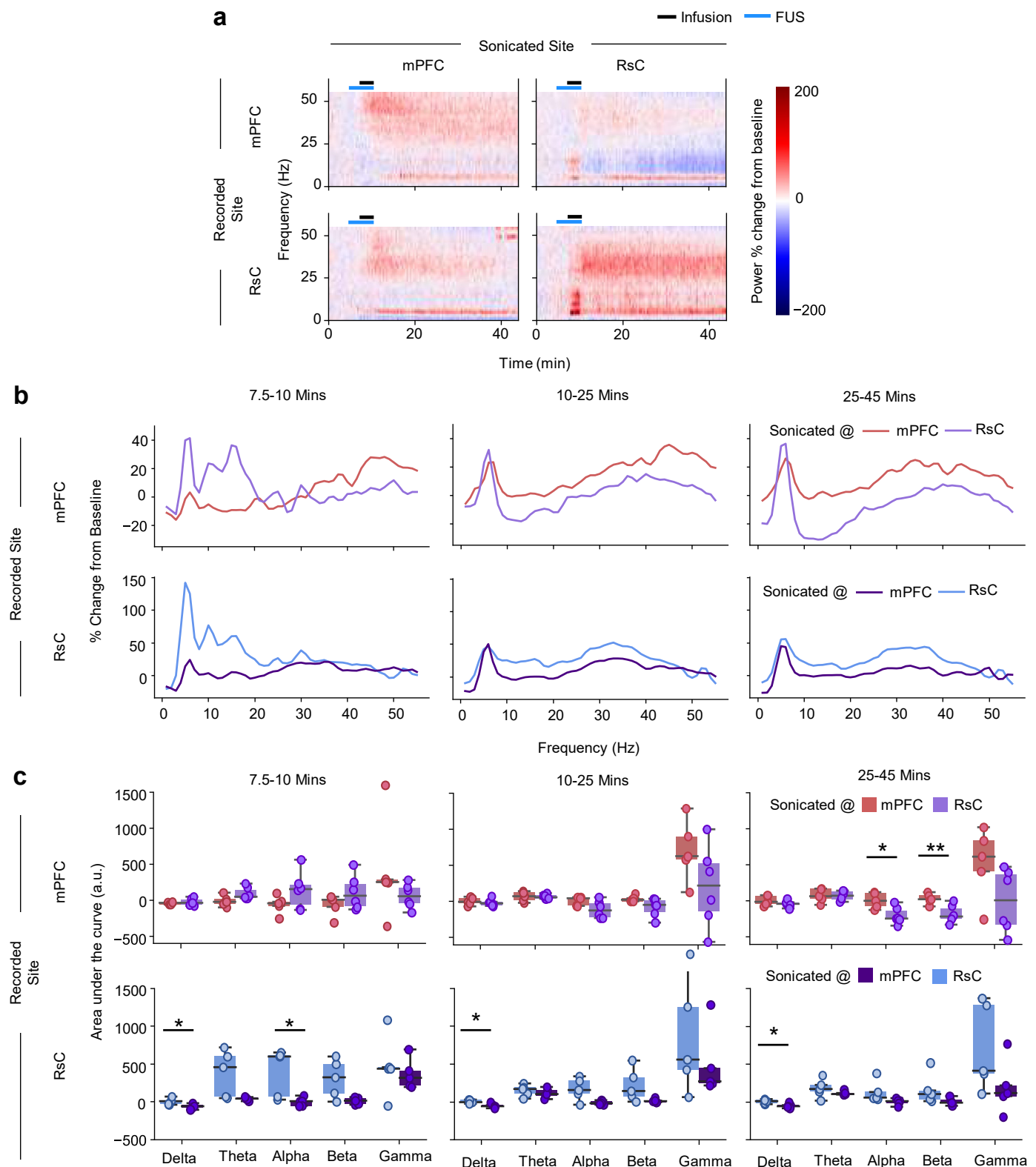
a. Ketamine quantification in blood samples collected at different timepoints after 1 mg/kg body weight intravenous bolus injection of free, unencapsulated ketamine-HCl or S5-KL ($n = 4$ adult rats each) shows differential blood clearance with S5-KL compared to free ketamine and its major metabolites norketamine and hydroxynorketamine (Quantification in Extended Data Table 3). **b.** Ketamine quantification in different organs after 60 min following 1.5 mg/kg body weight

intravenous bolus injection of free ketamine or S5-KL shows higher solid organ drug accumulation with ketamine-HCl compared to the ketamine-loaded AAL (S5-KL; $n = 4$ adult rats each). No significant differences of the metabolite solid organ uptake was noted between the formulations. Data presented as mean \pm SD. Comparisons between multiple groups performed by one way analysis of variance (ANOVA), ns = non-significant, * $p < 0.05$, ** $p < 0.01$ and *** $p < 0.001$.



Extended Data Fig. 5 | Rat brain electrophysiological dose-response analyses of Ketamine HCl i.v. infusion. **a.** Non-normalized time-frequency spectrograms of unencapsulated ketamine dose response recording from mPFC (top row) and RsC (bottom row) following 0.5, 0.75, 1, and 1.5 mg/kg i.v. infusion. **b.** Spectrograms of power percent change from the baseline (0-5 minutes of the

recording). **c.** Percent power change from baseline (0-5 min) versus frequency (Hz). Percent change was averaged within time bins during sonication (7.5-10 min), immediately after treatment (10-25 min), and after the clearance time point (25-45 min).



Extended Data Fig. 6 | Unique site-specific electrophysiological signals when recording from a different region than where sonication was applied.

a. Electrophysiological signals were recorded from either the mPFC or RsC after treatment with SonoKet and sonication either at the mPFC or the RsC. Spectrograms depicting electrophysiological response to SonoKet (0.75 mg/kg) with recording from the mPFC while ultrasound is applied to the mPFC (top left; $n = 5$; repeated from Fig. 4) or RsC (top right; $n = 6$); and recording from the RsC while ultrasound is applied to the mPFC (bottom left; $n = 5$) or RsC (bottom row; $n = 5$; repeated from Fig. 4). Power spectral density percent changes from

the baseline (0-5 mins) were calculated. **b.** Average percent change in power spectral density from baseline versus frequency for each of the three indicated time periods for each recording site and treatment: time of sonication (7.5-10 min), time immediately after treatment (10-25 min), and in a delayed period (25-45 min). **c.** Power spectral density percent change area under the curve for each spectral band: theta (4-8 Hz), alpha (8-15 Hz), beta (15-25 Hz), and gamma (25-55 Hz). Percent changes were calculated for each of the three indicated time periods. Data presented as box plots. Unpaired t-test, * $p < 0.05$, ** $p < 0.01$.

Reporting Summary

Nature Portfolio wishes to improve the reproducibility of the work that we publish. This form provides structure for consistency and transparency in reporting. For further information on Nature Portfolio policies, see our [Editorial Policies](#) and the [Editorial Policy Checklist](#).

Statistics

For all statistical analyses, confirm that the following items are present in the figure legend, table legend, main text, or Methods section.

n/a	Confirmed
<input type="checkbox"/>	<input checked="" type="checkbox"/> The exact sample size (<i>n</i>) for each experimental group/condition, given as a discrete number and unit of measurement
<input type="checkbox"/>	<input checked="" type="checkbox"/> A statement on whether measurements were taken from distinct samples or whether the same sample was measured repeatedly
<input type="checkbox"/>	<input checked="" type="checkbox"/> The statistical test(s) used AND whether they are one- or two-sided <i>Only common tests should be described solely by name; describe more complex techniques in the Methods section.</i>
<input type="checkbox"/>	<input checked="" type="checkbox"/> A description of all covariates tested
<input type="checkbox"/>	<input checked="" type="checkbox"/> A description of any assumptions or corrections, such as tests of normality and adjustment for multiple comparisons
<input type="checkbox"/>	<input checked="" type="checkbox"/> A full description of the statistical parameters including central tendency (e.g. means) or other basic estimates (e.g. regression coefficient) AND variation (e.g. standard deviation) or associated estimates of uncertainty (e.g. confidence intervals)
<input type="checkbox"/>	<input checked="" type="checkbox"/> For null hypothesis testing, the test statistic (e.g. <i>F</i> , <i>t</i> , <i>r</i>) with confidence intervals, effect sizes, degrees of freedom and <i>P</i> value noted <i>Give P values as exact values whenever suitable.</i>
<input checked="" type="checkbox"/>	<input type="checkbox"/> For Bayesian analysis, information on the choice of priors and Markov chain Monte Carlo settings
<input checked="" type="checkbox"/>	<input type="checkbox"/> For hierarchical and complex designs, identification of the appropriate level for tests and full reporting of outcomes
<input type="checkbox"/>	<input checked="" type="checkbox"/> Estimates of effect sizes (e.g. Cohen's <i>d</i> , Pearson's <i>r</i>), indicating how they were calculated

Our web collection on [statistics for biologists](#) contains articles on many of the points above.

Software and code

Policy information about [availability of computer code](#)

Data collection	Electrophysiology data was collected using the OpenBCI software.
Data analysis	GraphPad was used for statistical analysis. The K-Wave package in MatLab was used for ultrasound simulation analysis. The Noncompartment package in R studio was used for pharmacokinetics analysis. The MNE-Python package was used to analyze electrophysiology data. ToxTrac was used to analyze behavioral data. The BZ-X Advanced Analysis Software was used to analyze histological data. OpenLab from Agilent was used for HPLC data analysis and Zetasizer from Malvern was used for DLS data analysis. Agilent MassHunter software was used for LC-MS data acquisition and analysis.

For manuscripts utilizing custom algorithms or software that are central to the research but not yet described in published literature, software must be made available to editors and reviewers. We strongly encourage code deposition in a community repository (e.g. GitHub). See the Nature Portfolio [guidelines for submitting code & software](#) for further information.

Data

Policy information about [availability of data](#)

All manuscripts must include a [data availability statement](#). This statement should provide the following information, where applicable:

- Accession codes, unique identifiers, or web links for publicly available datasets
- A description of any restrictions on data availability
- For clinical datasets or third party data, please ensure that the statement adheres to our [policy](#)

Raw data underlying all figures and the code used to analyze the data are available via our GitHub repository (<https://github.com/Airan-Lab>). Any additional data not presented is available from the corresponding author upon reasonable request.

Research involving human participants, their data, or biological material

Policy information about studies with [human participants or human data](#). See also policy information about [sex, gender \(identity/presentation\), and sexual orientation](#) and [race, ethnicity and racism](#).

Reporting on sex and gender

Use the terms sex (biological attribute) and gender (shaped by social and cultural circumstances) carefully in order to avoid confusing both terms. Indicate if findings apply to only one sex or gender; describe whether sex and gender were considered in study design; whether sex and/or gender was determined based on self-reporting or assigned and methods used. Provide in the source data disaggregated sex and gender data, where this information has been collected, and if consent has been obtained for sharing of individual-level data; provide overall numbers in this Reporting Summary. Please state if this information has not been collected. Report sex- and gender-based analyses where performed, justify reasons for lack of sex- and gender-based analysis.

Reporting on race, ethnicity, or other socially relevant groupings

Please specify the socially constructed or socially relevant categorization variable(s) used in your manuscript and explain why they were used. Please note that such variables should not be used as proxies for other socially constructed/relevant variables (for example, race or ethnicity should not be used as a proxy for socioeconomic status). Provide clear definitions of the relevant terms used, how they were provided (by the participants/respondents, the researchers, or third parties), and the method(s) used to classify people into the different categories (e.g. self-report, census or administrative data, social media data, etc.) Please provide details about how you controlled for confounding variables in your analyses.

Population characteristics

Describe the covariate-relevant population characteristics of the human research participants (e.g. age, genotypic information, past and current diagnosis and treatment categories). If you filled out the behavioural & social sciences study design questions and have nothing to add here, write "See above."

Recruitment

Describe how participants were recruited. Outline any potential self-selection bias or other biases that may be present and how these are likely to impact results.

Ethics oversight

Identify the organization(s) that approved the study protocol.

Note that full information on the approval of the study protocol must also be provided in the manuscript.

Field-specific reporting

Please select the one below that is the best fit for your research. If you are not sure, read the appropriate sections before making your selection.

☒ Life sciences ☐ Behavioural & social sciences ☐ Ecological, evolutionary & environmental sciences

For a reference copy of the document with all sections, see nature.com/documents/nr-reporting-summary-flat.pdf

Life sciences study design

All studies must disclose on these points even when the disclosure is negative.

Sample size

All sample sizes were determined by power analyses of pilot data for each experiment.

Data exclusions

If any data were excluded from analysis the exclusion criteria are noted clearly in the methods.

Replication

To ensure reproducibility, each group average reported is the summary of independent samples of whole animals or whole replications of a particular in vitro assay.

Randomization

All sampling was completed randomly with blinded assortment of animals to treatment groups, and of independent randomized sampling of in vitro conditions.

Blinding

Particularly for in vivo experiments, analyses were completed blind to treatment condition either via an automated analysis pipeline that does not incorporate the group label, or via an observer rating behavioral data while blind to treatment conditions.

Reporting for specific materials, systems and methods

We require information from authors about some types of materials, experimental systems and methods used in many studies. Here, indicate whether each material, system or method listed is relevant to your study. If you are not sure if a list item applies to your research, read the appropriate section before selecting a response.

Materials & experimental systems

n/a	Involved in the study
<input checked="" type="checkbox"/>	<input type="checkbox"/> Antibodies
<input checked="" type="checkbox"/>	<input type="checkbox"/> Eukaryotic cell lines
<input checked="" type="checkbox"/>	<input type="checkbox"/> Palaeontology and archaeology
<input type="checkbox"/>	<input checked="" type="checkbox"/> Animals and other organisms
<input checked="" type="checkbox"/>	<input type="checkbox"/> Clinical data
<input checked="" type="checkbox"/>	<input type="checkbox"/> Dual use research of concern
<input checked="" type="checkbox"/>	<input type="checkbox"/> Plants

Methods

n/a	Involved in the study
<input checked="" type="checkbox"/>	<input type="checkbox"/> ChIP-seq
<input checked="" type="checkbox"/>	<input type="checkbox"/> Flow cytometry
<input checked="" type="checkbox"/>	<input type="checkbox"/> MRI-based neuroimaging

Animals and other research organisms

Policy information about [studies involving animals](#); [ARRIVE guidelines](#) recommended for reporting animal research, and [Sex and Gender in Research](#)

Laboratory animals	Long Evans rats between 7 -10 weeks old were used in all in vivo studies with ketamine. Sprague-Dawley rats between 7 – 10 weeks old were used in all in vivo studies with ropivacaine.
Wild animals	The study did not involve wild animals.
Reporting on sex	All in vivo experiments were performed with male rats.
Field-collected samples	The study did not involve field-collected samples.
Ethics oversight	All animal experiments were carried out in accordance with the Stanford IACUC and Administrative Panel 926 on Laboratory Animal Care (APLAC)

Note that full information on the approval of the study protocol must also be provided in the manuscript.

Plants

Seed stocks	N/A
Novel plant genotypes	N/A
Authentication	N/A